Title: **The Role of Physical, Numerical and Data Coupling in a Mesoscale Watershed Model**

Authors:

1) Mukesh Kumar
Research Assistant
212 Sackett Bldg.
Dept. of Civil and Environmental Engineering
Penn State University, University Park, 16802
muk139@psu.edu

2) Gopal Bhatt
Research Assistant
212 Sackett Bldg.
Dept. of Civil and Environmental Engineering
Penn State University, University Park, 16802
gxb913@psu.edu

3) Christopher J. Duffy (Corresponding Author)
Professor
212 Sackett Bldg.
Dept. of Civil and Environmental Engineering
Penn State University, University Park, 16802
cxd11@psu.edu

Keywords: PIHM; PIHMgis; Integrated Hydrologic Model; Unstructured Mesh; Little Juniata Watershed; Finite Volume; Stream Aquifer Interaction

Abstract

Full coupling of physical processes, natural numerical coupling, and parsimonious but accurate data coupling are three key steps in efficient and accurate simulation of distributed hydrologic states in watersheds. Here we present a physically-based, spatially distributed hydrologic model (called PIHM) that utilizes all the three coupling strategies. Interception, snow melt, transpiration, evaporation, overland flow, subsurface flow, river flow, macropore based infiltration and lateral stormflow, as well as flow through and over hydraulic structures such as weirs and dams are some of the physical processes handled in the model. A semi-discrete, Finite-Volume approach is used to define the distributed process equations on discretized unit elements, in terms of a fully-coupled system of ordinary differential equations. An implicit Newton-Krylov based solver that utilizes adaptive time stepping provides a robust and stable solution. Data-coupling is aided by the use of constrained unstructured meshes, and a flexible data model incorporated within an open-source GIS tool (PIHMgis). The spatial adaptivity of the mesh elements and temporal adaptivity of the numerical solver facilitates capture of multiple spatio-temporal scales, allowing important insight into hydrologic process interactions. The implementation of the model has been performed for a mesoscale watershed in central PA (Little-Juniata Watershed, 845 km^2). Model results are validated by comparison of observed and predicted streamflow and groundwater levels at multiple locations. The fully-coupled model unfolds a range of multiscale/multiprocess interactions including: 1) an apparent inverse relationship between fraction of total evapotranspiration rate due to transpiration and interception loss, 2) the role of forcing (precipitation, temperature and radiation), soil moisture and overland flow on evaporation-transpiration partitioning, 3) the importance of water table depth on evaporation-transpiration, 4) the influence of local upland topography and stream morphology on spatially distributed, asymmetric right-left bank river-aquifer interactions, and, 5) the role of macropore and topography on ground water recharge magnitude, time scale and spatial distribution.

1. Introduction

Surface water, plant water, soil and groundwater, and the atmosphere are linked components of a hydrologic continuum. Changes in one affect the other on a variety of spatio-temporal scales. These interactions are influenced by the different components of the "hydrogeologic environment" [73],[43] such as vegetation, topography, geology and climate. Clearly, vegetation influences the distribution and rates of water due to a wide range of processes, including interception, stemflow and transpiration [9], [37] and also contributes to formation of root holes which serve as flow ducts for macroporous infiltration and stormflow [80] particularly in forested catchments. By considering five watersheds with topography and geology varying from glacial, coastal, wetland, karst and riverine, and climate varying from semi-arid to humid Winter [81] observed that local physiographic controls significantly influence the magnitude and direction of interaction between surface and ground water. Sometimes the interactions also modify or interact with the macro-scale hydrogeologic environment resulting in formation of wetlands [34], river meanders [60] and floodplains [56].

On the computational side, numerical modeling efforts which focus on simulating individual processes have made significant progress in recent years. Studies by Gottardi and Venutelli [31] and, Feng and Molz [28] for overland flow runoff; USACE-UNET [75], and Strelkoff [72] for flow in rivers and Huyakorn et al. [40] and Paniconi and Wood [59] for modeling saturated–unsaturated flow in the subsurface provide good examples. More recently, distributed and fully coupled approaches to watershed/river basin simulation have become a major research effort. Perkins and Koussis [5], Govindraju and Kavvas [32] are examples of coupled surface-subsurface flow by considering the land surface as a boundary through which a flux exchange takes place. In these papers, it was observed that coordinating the interaction between coupled models at artificial internal boundaries posed a severe numerical challenge for transient system responses. Similar observations were also made by Brown [12] who experienced numerical difficulty in partitioning of rainfall between the microporous soil matrix and macropores and Refsgaard and Storm [63] who reported problem in convergence in MikeSHE [1] because of the need for synchronization of time steps for different flow components. According to Fairbanks et. al.[27], attempts at coupling hydrologic processes where each of the flow processes are simulated separately, using independent time steps and a mixture of explicit and implicit techniques such as in models like Tribs [41] results in numerically weak, inaccurate and unreliable solutions. Of the three established coupling methods [46] viz. a) a sequentially coupled approach in which the head for one system acts as a general-head boundary for the other system (b) a sequentially coupled approach in which the interaction flux is applied as a boundary condition to each model and (c) a 'fully coupled' or 'fully implicit' approach, the last one was found to be most robust and accurate [27]. The fully coupled solution also outperforms linked/iteratively coupled methods in terms of computational efficiency for highly interactive systems.

Apart from considering multiple processes and full numerical coupling, another important problem for hydrologic simulation involves striking a balance between grid size or process resolution and the scale of computation [50]. Models based on structured grids are limited in terms of ingesting fine physiographic details particularly of linear features like rivers and watershed boundaries. This is due to the rigidness of a structured grid in terms of its shape, regularity and orientation in two principal directions only. Terrain and hydrographic features that are not oriented along any of the axes of rectangular grids are difficult to resolve without resorting to high spatial resolution discretization of the entire model domain or performing localized adaptive mesh refinement [7]. Vivoni et. al. [79], Kumar et. al. [50], and Qu and Duffy [61] have discussed the advantages of using Triangular Irregular Networks (TINs) and unstructured meshes over structured grids in terms of computational efficiency, flexibility and accuracy for hydrologic modeling. Among the new generation of physically based distributed hydrologic models such as InHM [77], MIKE SHE [33], MODHMS [58], PARFLOW-Surface Flow [48] and WASH123D [83], InHM and WASH123D use finite element methodology to solve for states on unstructured grids.

This paper details the physical, numerical and data coupling framework of the Penn State Integrated Hydrologic Model (PIHM). All coupled hydrologic processes (evaporation, interception, snow-melt, overland flow, river flow, subsurface flow and macropore flow) are solved using a fully coupled numerical strategy on unstructured meshes. Spatial adaptivity of unstructured grids and temporal adaptivity of the numerical solver helps to resolve the full range of scales of process interactions over a simulation period. The model application is performed for a 2 year period in the Little Juniata watershed with area of 845 km^2.

2. Data Coupling: An Integrated Framework

A data model is a useful way to incorporate a large number of physical data layers into the modeling framework, including topology definitions. Here we use a flexible "shared" data-model to enhance the access of raw GIS data structures directly by the hydrologic model, thus reducing the model setup time, and facilitating data integrity and concurrent data access [51]. The integration framework uses the data-model to define relationships between different data types and their relation to the physical model environment (discretized hydrologic domain). The framework supports all scales of hydrologic interactions by using adaptively constructed grids to capture the heterogeneity in the domain physical properties and processes. The decomposition grids are constrained Delaunay triangulations which facilitate efficient ingestion of different physical parameter fields, simply and accurately from a geodatabase. Some common constraints used during grid generation involve point constraints such as stream gage locations, weirs, VIPs (i.e.. Very Important Points after Chen and Guevara [15]), groundwater well locations, and line constraints such as subwatershed boundaries, land cover, and soil type. The advantage of point and line constraints is in reducing errors due to interpolation or geo-referencing of modeled data to observations. For example, Fig. 1 shows a domain decomposition of Little Juniata Watershed with and without constraints. The decomposition shown on left does not include observation stations as constraints, while the decomposition on the right does. This means that hydrologic states will be predicted exactly at the observation stations in the second case. Decomposition based on a line constraint also limits model parameterization errors. A parameter such as land cover or soil type can be used as a boundary or edge, defined by the sides of triangular elements. This ensures that a single land-cover/soil class exists within an unstructured mesh element thus limiting introduction of any additional uncertainty because of statistical averaging of multiple class types within an element [50]. For unconstrained situations, say when land-cover or soil classes are not used as a constraint, a mean parameter or statistic can be specified. Local boundary constraints during decomposition can be used to specify regions with smaller mesh size, where faster hydrodynamics, steeper topography, or atmospheric forcing effects are expected. Similarly, meshes generated along the river can be designed to better capture the riparian dynamics and flood plain inundation. Apart from its advantage of computational efficiency and spatial adaptivity, unstructured meshes can be tailored to the complex geometries and physics of a given problem [50]. Algorithms for generating unstructured meshes using GIS feature objects and the advantages of resulting triangulations are discussed in Kumar et. al. [50].

Once the decomposition has been performed, soil, vegetation and hydrogeologic data is assigned to each element in the mesh. In many cases, the data must be viewed, queried, analyzed or sometimes even reused while the simulation proceeds. Traditionally this step has been addressed using existing GIS tools and feeder data access interfaces. Here we have used the tightly coupled integrated framework called PIHMgis to manage, analyze, visualize and to define relationships between hydrographic units and their physical properties. Details of the GIS-PIHM integration (PIHMgis) can be found in Bhatt et. al. [6].

3. Physical Coupling: Semi-Discretized Process Equations

PIHM uses a semi-discrete finite volume formulation for coupled hydrologic processes [61]. A generalized partial differential equation (PDE) of flow of a conservative scalar variable ψ in the hydrologic system is universally expressed as

$$\frac{\partial \psi}{\partial t} = \nabla(\psi U) + \nabla(\Gamma grad\, \psi) + S_\psi \tag{1}$$

or the rate of change in ψ = (Convective Flux) + (Diffusive Flux) + (Source/Sink), where U is the velocity vector, Γ is conductivity and S_ψ is rate of increase/decrease in ψ due to sources/sinks. The system of process defining PDEs is then locally reduced to ordinary differential equations (ODEs) by integration on a spatial unit element. The PDEs are integrated over an arbitrary three dimensional control volume, V_i in the model domain as

$$\int_{V_i} \frac{\partial \psi}{\partial t} dV = \int_{V_i} \nabla(\psi U) dV + \int_{V_i} \nabla(\Gamma grad\, \psi) dV + \int_{V_i} S_\psi dV \tag{2}$$

By applying Gauss's theorem on the convective and diffusive term on the right hand side of the Eq. (1), we obtain

$$\frac{\partial}{\partial t}\int_{V_i} \psi dV = \int_{A_{ij}} N.(\psi U) dA + \int_{A_{ij}} N.(\Gamma grad\, \psi) dA + \int_{V_i} S_\psi dV \tag{3}$$

where N is the normal vector to the surface j of the control volume V_i. As mentioned in the previous section, PIHM discretizes the watershed domain into unstructured elements (prismatic in 3D) and the river into linear elements (rectangular/trapezoidal in 3D), as shown in Fig. 2. This translates to the number of boundary faces j = 5 for prismatic elements and j = 6 for river elements. For notational simplicity, we represent convective flux (ψU) as $\vec{C}_f$ and separate diffusive flux ($\Gamma grad\, \psi$) into vertical ($\vec{G}$) and horizontal fluxes ($\vec{F}$) respectively. This reduces Eq. (3) into

$$\frac{\partial}{\partial t}\int_{V_i} \psi dV = \int_{A_{ij}} N.(\vec{C}_f) dA + \int_{A_{ij}} N.(\vec{G} + \vec{F}) dA + \int_{V_i} S_\psi dV \tag{4}$$

By integrating the individual terms in Eq. (4) and approximating the governing equation by its diffusive equivalents only (in this case by setting $\vec{C}_f$ = 0), we obtain a generic semi-discrete form of ODE that defines all the hydrologic processes incorporated in the finite volume of the model as

$$A_i \frac{d\overline{\psi}}{dt} = \sum_j N.\vec{G} A_{ij} + \sum_k N.\vec{F} A_{ik} + \overline{S}_\psi V_i \tag{5}$$

where $\overline{\psi}$ (L) is the average volumetric conservative scalar per unit planimetric control volume area A_i and $\overline{S}_\psi$ is the average source/sink rate per unit control volume. Every prismatic volume (kernel) is a stack of 5 control volumes (Fig. 2). Eq. (5) represents the state variables coupled through vertical flux ($\vec{G}$) and lateral horizontal flux ($\vec{F}$) terms. Similarly a river or channel kernel consists of 2 control volumes as shown in Fig. 2. Table 1 lists the vertical and horizontal flux terms associated with each state and identifies the coupled flux interactions between neighboring control volumes (both in vertical and in horizontal) through a process coupling function $f[]$. Individual vertical, horizontal and source/sink flux terms listed in Table 1 can be directly replaced in Eq. (5) to evaluate the respective state equations. The coupling function $f[]$ defined in Table 1 shows that the coupling between processes such as interception-snow, interception-unsaturated zone is "one-way" only, while interactions between unsaturated-saturated and river-saturated zone are "two-way". Explanations of the symbols not described in the text can be referred to in Appendix I. Details of the vertical, horizontal and source/sink flux term calculations listed in Table 1 are discussed next.

3.1. Throughfall Drainage

The rate of throughfall drainage ($\vec{G}_5$) depends on the interception storage depth (ψ_0) by

$$\begin{aligned} \vec{G}_5 &= k \exp[b(\psi_0 / \psi_{0\max})] \text{ for } 0 \le \psi_0 < \psi_{0\max} \\ &= k \exp[b] \text{ for } 0 < \psi_{0\max} \le \psi_0 \end{aligned} \tag{6a}$$

where $\psi_{0\max}$ is the canopy water storage capacity (L)

The drainage parameter b (dimensionless) and k (LT^{-1}) are based on Rutter and Morton [66], who suggested b ranging from 3.0 to 4.6, and k = 3.91 x $10^{-5}\psi_0$ (in mm/min). $\psi_{0\max}$ depends on LAI as

$$\psi_{0\max} = K_L \text{ x } LAI \tag{6b}$$

where K_L is assumed to be 0.2 mm [22]. We note that the calculations performed above are "physically based" only in weak sense as they do not take into account the complex canopy architecture and so will be accurate for limited ranges of vegetation types and spatial scales. The ODE defining the changes in the depth of the water stored in the canopy is described by

$$\frac{d\psi_0}{dt} = (\vec{G}_3 - \vec{G}_4 - \vec{G}_5) \tag{6}$$

where $\vec{G}_3$ is $vFrac*(1-f_s)$ times the precipitation rate (LT^{-1}), $\vec{G}_4$ is evaporation from canopy storage (LT^{-1}), $vFrac$ is fractional areal vegetation cover in a control volume and f_s is snow fraction.

3.2. Evapotranspiration

Total evapotranspiration (ET) is the sum of evaporation [70] from the upper soil layer ($\vec{G}_8$), from overland flow ($\vec{G}_7$), from evaporation of interception ($\vec{G}_4$), and transpiration ($\vec{G}_9$). Total evapotranspiration is expressed as

$$\mathrm{ET} = \vec{G}_4 + \vec{G}_7 + \vec{G}_8 + \vec{G}_9 \tag{7}$$

The vertical flux components in Eq. (7) are calculated as follows:

$$\vec{G}_7 = (1 - vFrac)\frac{Q^*\Delta + (\rho C_{pa}/r_a)(e_{sz} - e_z)}{\Delta + \gamma} \tag{7a}$$

$$\vec{G}_8 = \beta_s \vec{G}_7 \tag{7b}$$

$$\beta_s = \begin{cases} 0.5(1 - Cos[\pi(\dfrac{\theta_g}{\theta_{fl}})]) & \theta_g \le \theta_{fl} \\ 1 & \theta_g > \theta_{fl} \end{cases}$$

where $\theta_{fl} = 0.75\theta_{sat}$ is the field capacity, θ_{sat} is saturated moisture content, θ_g is moisture content of the top soil layer and β_s describes the influence of the top soil layer saturation on evaporation from ground [69]. We note that saturation of the top soil layer is related to ψ_3 though van-Genuchten relationship (Eq. 11a). Evaporation from the wet canopy is calculated by

$$\vec{G}_4 = vFrac\frac{Q^*\Delta + (\rho C_{pa}/r_a)(e_{sz} - e_z)}{\Delta + \gamma}\delta_r \qquad \delta_r = (\frac{\psi_0}{\psi_{0\max}})^{\frac{2}{3}} \tag{7c}$$

where δ_r is the area fraction of the wet canopy as calculated in [21]. Sub-linear dependence of δ_r on the ratio of ψ_0 to $\psi_{0\max}$ captures the increasing rate of evaporation of canopy water as the fraction of leaf area containing water decreases. Vegetation also influences ground-water by extraction of soil water by transpiration thus decreasing the amount of percolating water that reaches the saturated zone and increasing the capillary rise. Based on the formulation of [8], transpiration is independently calculated by

$$\vec{G}_9 = vFrac\frac{Q^*\Delta + (\rho C_{pa}/r_a)(e_{sz} - e_z)}{\Delta + \gamma(1 + \dfrac{r_s}{r_a})}(1 - \delta_r) \tag{7d}$$

The bulk stomata resistance, r_s (TL^{-1}) of the canopy due to specific humidity gradient between leaves and overlying air depends largely on the minimum resistance, the available solar energy, the availability of water in the root zone and the air temperature [42]. In PIHM, r_s is obtained based on [22] as

$$r_s = \frac{r_{\min}\alpha_r\beta_s}{LAI\eta_s^{\,4}} \qquad \text{where } \alpha_r = \frac{1 + f_r}{1 + r_{\min}/r_{\max}} \text{ and } f_r = \frac{1.1R_{sc}}{R_s^{\,ref}\,LAI} \tag{7e}$$

where R_{sc} (MT^{-3}) is estimated by Beer's law as

$$R_{sc} = R_s(1 - \exp(-\alpha LAI)) \tag{7f}$$

and R_s^{ref} (MT^{-3}) is assumed as 30 Wm^{-2} for trees and 100 Wm^{-2} for grassland and crops [10]. β_s is the saturation in the active soil layer (Eq. 7b) for agricultural and pasture land and in the transmission zone for forest, controlled by root depth of each vegetation type. η_s accounts for the reduced activity of plants when the air temperature is very high or very low and is calculated according to

$$\eta_s = 1 - 0.0016(298.0 - T_a)^2 \tag{7g}$$

$r_{\max}$, maximum stomata resistance is set uniformly to 5000sm^{-1}. $r_{\min}$ is minimum stomata resistance. For the simulation performed here, $r_{\min}$ is obtained from the vegetation parameters used in LDAS as available on [47].

3.3. Snow Melt

The basic snow melt ($\vec{G}_6$) flux is based on a temperature index model equation represented by

$$\vec{G}_6 = C_s(T_a - T_b) \tag{8a}$$

The melt rate coefficient C_s typically varies between 1.8 to 3.7 mm/^{o}C. Air temperature is used to partition snow and rain [74] according to

$$f_s = \begin{cases} 1.0 & T_a < T_s \\ \dfrac{T_r - T_a}{T_r - T_s} & T_s \le T_a \le T_r \\ 0 & T_a > T_r \end{cases} \tag{8b}$$

where T_r (=1^{o}C) is the air temperature above which all precipitation is assumed to fall as rain, and T_s (=-3^{o}C) is the air temperature below which all precipitation is assumed to fall as snow. The semi-discrete ODE representation of snow accumulation/melt is represented by

$$\frac{d\psi_1}{dt} = (\vec{G}_3 - \vec{G}_6) \tag{8}$$

where $\vec{G}_3$ is f_s times the precipitation rate (LT^{-1}).

3.4. Infiltration

Infiltration ($\vec{G}_0$) is handled according to the approach of Freeze [29] by

$$\vec{G}_0 = \Gamma\, grad\, \psi \tag{9}$$

where

$$\Gamma = K(\psi_3) \qquad grad\,\psi = \frac{(\psi_2 + z) - (\psi_3 + z_u)}{d} \tag{9a}$$

$K(\psi_3)$ is the vertical hydraulic conductivity of the top soil layer [L/T], z is the land surface elevation, z_u the elevation of the top soil layer and d is a specified vertical distance across which the head gradient is calculated. This coupling strategy is based on continuity in hydraulic head across the surface skin thickness ($2d$). $K(\psi_3)$ is calculated using van Genucten equation (discussed later in Eq. 11a).

3.5. Unsaturated-Saturated Flux

The ODE defining the change in unsaturated zone soil moisture depth is given by

$$\frac{d\psi_3}{dt} = \vec{G}_0 - \vec{G}_1 \tag{10}$$

Flux between saturated-unsaturated zones is calculated using Richard's equation [62] by assuming a vertical exchange across a moving boundary (water table interface). The approach is similar to [25]. The vertical flux at the water table can be approximated by (derivation details in Appendix III):

$$\vec{G}_1 = \frac{K_u(\psi_3)K_s z_b(\alpha(z - z_b - \psi_4) - 2(-1 + S^{\frac{n}{1-n}})^{\frac{1}{n}})}{\alpha(K_u\psi_4 + K_s(z - z_b - \psi_4))} \tag{11}$$

where $K_u(\psi_3)$ and S of the unsaturated zone is calculated according to van Genuchten [78] equation as

$$K_u(\psi_3) = S^{0.5}(1 - (1 - S^{\frac{n}{n-1}})^{\frac{n-1}{n}})^2 \text{ and } S = \frac{\psi_3}{z - z_b - \psi_4} \tag{11a}$$

α and n in the above equations are van Genuchten' soil retention parameters. Similar derivations for vertical flux using other $K_u - S$ relationships from Brooks-Corey [11], Srivastav and Yeh [71] are also incorporated in the model.

3.6. Groundwater Flow

Lateral ground water flow $\vec{F}_2$ is governed by Darcy-type flow and the conductance and gradient terms between neighboring control volumes (shown in Fig. 3) are evaluated as

$$\Gamma = K_{eff} \qquad grad\,\psi_{ij} = \frac{(\psi_{4i} + z_{bi}) - (\psi_{4j} + z_{bj})}{d_{ij}} \tag{12a}$$

The ODE for head in saturated zone is written as

$$\frac{d\psi_4}{dt} = \vec{G}_1 + \frac{1}{A}\left(\sum_{j=1}^{3} UW[\psi_{4i}, \psi_{4j}]e_j\Gamma_j\, grad\,\psi_{ij}\right). \tag{12}$$

3.7. Surface Overland Flow

The transient flow of water on the land surface ($\vec{F}_0$) is estimated by either a kinematic wave or diffusion wave approximation to the depth-averaged shallow water equations. Assuming a negligible influence of inertial forces and shallow depth of water ψ_2(L), the conductivity, Γ and gradient term, $grad\,\psi$ in Eq. (3) for the diffusion wave approximation of St. Venant's equation is calculated using Gottardi and Venutelli [31] by

$$\Gamma = \frac{\psi_{2i}^{2/3}}{n_s}(\nabla_s(\psi_{2i} + z_i))^{-\frac{1}{2}} \text{ and } grad\,\psi_{ij} = \frac{(\psi_{2i} + z_i) - (\psi_{2j} + z_j)}{d_{ij}} \tag{13}$$

where $\nabla_s \psi$ is the gradient of overland flow head in the direction of maximum slope. $\nabla_s \psi$ for a triangular element is approximated by calculating the slope of the triangular stencil [57] shown in Fig. 4. We reiterate at this point that overland flow flux is calculated between all neighboring elements of a triangle according to Eq. (4). The maximum slope calculation is performed only to calculate the diffusive conductivity term in (13). Details of the slope calculation can be found in Appendix II. We note that for triangular elements that are adjacent to channels, the triangular slope stencil is bounded by a channel element and the calculation of slope uses total heads from two neighboring triangular elements and a channel as shown in Fig. 4. Substituting the simplified conductivity and gradient relationships of Eq. (13) in Eq. (5) adequately resolves backwater effects and is applicable to flow on flat surfaces [23]. The kinematic wave approximation requires a different conductance term given by $\Gamma = \frac{\psi_2^{2/3}}{n_s^{1/2}} \nabla_s z$. The kinematic approximation while supported in PIHM is not considered in the simulations presented in this study. The semi-discrete ODE for overland flow depth reduces to

$$\frac{d\psi_2}{dt} = (\vec{G}_3 - \vec{G}_7 + \vec{G}_5 + \vec{G}_6) - \vec{G}_0 + \frac{1}{A_i}\Big(\sum_{j=1}^{3} \vec{F}_{0j} UW[\psi_{1i}, \psi_{1j}] e_j + \left\| \vec{F}_1((\psi_{1i} + z_i) - (\psi_{5j} + z_{rj})) L_j \right\| \Big) \tag{14}$$

where $\vec{G}_3$ is (1-$vFrac$) times the precipitation rate (LT^{-1}). We note that $\| \; \|$ are conditional terms which exist only for the grids that are neighbor of a river element. The flux of overland flow across river banks, $\vec{F}_1$, is defined in the next section. $UW[]$ is an upwind function which identifies the upstream head or flow-depth (out of its two arguments) for overland flow (and also for channel and groundwater flow that are discussed later in the text). For an overlandflow case, gradient of total overland flow head is considered positive from upstream to downstream.

3.8. Surface Overland Flow to River

Surface flow across the channel banks ($\vec{F}_1$) is calculated using Robertson [65] as

$$\vec{F}_1 = C_d \frac{2}{3}\sqrt{2g}\,((\psi + z)_u - \max[(\psi + z)_d, z_{rb}])^{1/2} \tag{15}$$

where $(\psi + z)_u$ and $(\psi + z)_d$ are the upwind and downwind head respectively as characterized by whichever is the higher and lower head that exists across the channel bank. The downwind head is a boolean choice between total streamflow head head and river bank elevation depending on whether the bank is submerged or not as depicted in Fig. 5.

3.9. Channel Flow

Flow through a network of rivers and channels are characterized by the one-dimensional diffusion/kinematic wave approximation to the St. Venant equations. The conductance and gradient terms are derived in a similar manner as in Eq. 10 as

$$\Gamma = \frac{\psi_5^{\;2/3}}{n_s}\left(\nabla(\psi_5 + z_r)\right)^{-\frac{1}{2}} \qquad grad\,\psi_{ij} = \frac{(\psi_{5\,i} + z_{r\,i}) - (\psi_{5\,j} + z_{r\,j})}{d_{ij}} \tag{16}$$

The semi-discrete ODE defining the river flow is represented as

$$\frac{d\psi_5}{dt} = \frac{1}{A_i}\left(\sum_{j=1}^{2}\Gamma_j\, grad\,\psi_{ij} UW[\psi_{5i}, \psi_{5j}]e_j + \sum_{j=1}^{2}\vec{F}_{1j}(UW[\psi_{2j} + z_j, \psi_{5i} + z_{ri}]L_i)\right)$$
$$+\frac{1}{A_i}\sum_{j=1}^{2}\vec{F}_{3j}(UW[\max[\psi_{4j} + z_{bj} - z_{ri}, 0], \psi_{5i}]L_j) - \vec{G}_2 + \vec{G}_3 - \vec{G}_7 \tag{17}$$

where $\vec{G}_3$ is precipitation on the river surface.

3.10. Channel and Aquifer Interaction

The channel interacts with aquifer through its bed and edges as shown in Fig. 2. Lateral flux exchange through the channel edges can be calculated by

$$\vec{F}_3 = \Gamma grad\,\psi_{ij} \tag{18}$$

where conductance and gradient terms are

$$\Gamma = K_{eff} \qquad grad\,\psi_{ij} = \frac{(\psi_{5i} + z_{ri}) - (\psi_{4j} + z_{bj})}{d_{ij}} \tag{18a}$$

Flux exchange through the river bed follows the same equations as (18a) until the river aquifer becomes hydraulically disconnected after which the gradient is dependent on the head in river only [64].

3.11. Sub-Channel Groundwater Flow

Ground water flow beneath the river interacts with the river as well as the neighboring aquifer elements. Gradient and conductance terms along and lateral to the channel are calculated as

$$\Gamma = K_{eff} \qquad grad\,\psi_{ij} = \frac{(\psi_{6i} + z_{bi}) - (\psi_{6j} + z_{bj})}{d_{ij}} \tag{19a}$$

$$\vec{F}_4 = K_{eff}\,\frac{(\psi_{6i} + z_{bi}) - (\psi_{4j} + z_{bj})}{d_{ij}} \tag{19b}$$

The ODE defining the flow is written as

$$\frac{d\psi_6}{dt} = \frac{1}{A_i}\sum_{j=1}^{2}\Gamma_j\, grad\,\psi_{ij} UW[\psi_{6i}, \psi_{6j}]e_j$$
$$+\frac{1}{A_i}\sum_{j=1}^{2}\vec{F}_{4j}(UW[\min[\psi_{4j}, z_{ri} - z_{bj}], \psi_{6i}]L_j + \vec{G}_2 \tag{19}$$

3.12. Macropore Infiltration

Preferential flow through macropores in forested catchments such as root holes, cracks or pipes in soils, or through dissolution features, joints, and fractures in bedrock lead to large and fast infiltration and recharge to groundwater [2]. These macroporous features may result in bypassing of most of the infiltration from the surface soil layer directly to deeper layers. Even though the macroporous volume is small relative to the soil matrix (~ 1 % of the pore volume), the volumetric transport capacity can be significant to the overall flow. The critical pore size at which infiltration can be classified as macropore flow has been discussed in Beven and Germann [4].

Several studies have focused on approximating the macropore flow contributions to subsurface flow [39]. Vanderkwaak [77] used a dual continua approach by calculating heads and interacting fluxes in macropores and soil matrix separately and assuming Richard's equation to be valid in each of them. Gerke and van Genuchten [30] and Mohanty et al. [53] studied the effect of macropores on soil hydraulic properties using multi-domain models. Here we follow a simpler dual-domain approach [36]. The approach represents an equivalent matrix-macropore system that is assumed to follow Richard's equation with total infiltration/exfiltration rate to be equal to sum of matrix infiltration ($\vec{G}_{0mat}$) and macropore infiltration ($\vec{G}_{0mac}$) as shown in Fig. 6. The net conductivity of the equivalent system is determined by the head difference that exists across the infiltration layer [16] as shown in Table 2. $\vec{G}_0$ and $grad\,\psi$ in Table 2 are calculated according to Eq. (9) and

$$K_{\max} = K_{matV}[S](1-\beta) + K_{macV}\,\beta \qquad (20)$$

We note that the conditional statement in the second row (in Table 2) means that if the water application rate on the soil surface is less than the hydraulic conductivity of the matrix, the water flow rate through the equivalent system will be limited by the application rate and the equivalent conductivity will be equal to the matrix conductivity at a given saturation. The third row defines the conductivity when the infiltration rate is greater than the conductivity of the soil matrix but less than $K_{\max}$. The last row is the equivalent conductivity when the application rate is greater than $K_{\max}$. In this case water will flow through both the matrix and macropores with majority of the flow contributed through macropores.

3.14. Macroporous Stormflow

In addition to the increase in soil infiltration capacity, a second effect of a macroporous soil is the possible lateral conduction of subsurface stormflow [55]. A macropore system with sufficient connectivity over a particular soil depth and distance leads to quick transmission of soil water as subsurface stormflow or interflow. The depth of this interflow layer is assumed to be the depth of the macroporous soil, which will depend on the vegetation type and root distribution, organic content and geologic structure. The net conductivity for lateral flow is dependent on the macroporous soil thickness and soil saturation given by:

$$K_{eq} = K_{matH}[S](1-\beta) + K_{macH}[S]\beta \tag{21}$$

The percentage of macropore that becomes active is assumed here to be linearly dependent on the average saturation of macroporous soil layer i.e.

$$K_{macH}[S] = K_{macH}[S=1].S \tag{21a}$$

Given the relatively coarse spatial discretization that is used in the model application, lateral flow through karst fractures can be modeled as subsurface stormflow.

3.15. Specified Flux or Head Conditions

Specified flux, hydraulic head or mixed boundary conditions are implemented for watershed boundaries, river outlets, injections/withdrawals/controls and hydraulic structures like weirs, wells, dams etc. Dirichlet, Neumann or Cauchy boundary conditions [54] can be applied to any of the state variables on any of the element edges, both prismatic watershed elements and linear river elements. Typically specified conditions incorporated in PIHM are a) flow/no-flow condition (at watershed boundaries), b) critical depth boundary condition (at weirs, falls or flow into deep lakes) given by

$$\vec{F}_5 = \sqrt{g(\psi_5 - z_w)} \tag{22a}$$

where z_w is the height of weir and c) zero-gradient boundary condition (at the channel outlet in alluvial plans) given by

$$\vec{F}_5 = \frac{1}{n}\left(\frac{A}{P}\right)^{2/3} S_o^{\;1/2} \tag{22b}$$

where A is the cross-sectional area of channel, P is wetted perimeter and S_o is the slope of the bed.

4. Numerical Coupling: Solution Strategy and Kernel Flexibility

The local coupling of ODEs corresponding to each physical process forms the model *kernel* within the prismatic 3D element. Assembling the kernel over the model domain forms the global ODE system, assuring a fully coupled or direct numerical coupling procedure. All state variables are solved simultaneously and advance together at each time step. The time step is adaptively determined by the fastest time scale of the interacting processes. The strategy requires a stiff solver. Appendix IV details the mathematical explanation of stiffness arising in a representative coupled system and explains the limitation of the explicit solution methodology to solve such a system.

4.1. Numerical Solver

The Newton–Krylov implicit solver is a typical choice for large non-linear stiff ODE system [44], [45]. Here we use the CVODE solver [17] from the SUNDIALS package to solve the system of stiff ODEs. CVODE uses a combination of the Backward Difference Formula (BDF) with linear Krylov iteration, and a preconditioned GMRES algorithm [14]. Adaptive time-stepping and an order-adjustment scheme alleviate the computational burden posed by the implicit solver. The internal time steps taken by the solver becomes smaller in response to rapid changes in state triggered by precipitation events. Large precipitation events lead to generation of overland flow, resulting in increased interaction of surface-subsurface processes, thus further increasing the stiffness of ODE system. The solvers' treatment of stiff terms provides solutions which are accurate at slow scales and stable at fast scales (due to channel flow, overland flow and stream-aquifer interactions).

4.2. Kernel Flexibility

An important feature of the PIHM formulation is that its data structure remains isolated and independent from CVODE’s data structure. This approach allows the user to easily alter the system of equations in the kernel without having to manually change the numerical discretization. Multiple formulations can be activated simply using boolean switches on the right hand side of ODE. This provides the user a unique flexibility in the choice of process equations used in a particular kernel, depending on the model purpose or other computational constraints. As an example, for modeling large western watersheds with mountainous upland topography with dry valleys, the snow-melt process can be removed over part of the domain. The simplicity of using a “switch” without having to reformulate the numerical discretization is also useful for testing trial constitutive relationships and new theoretical formulations.

5. Model Application: Site Description and Data Needs

Application of the PIHM model has been carried out for the Little Juniata River Watershed, located in south central Pennsylvania. The watershed size is 845.6 sq. km and is within the US National Weather Service (NWS) mid-Atlantic river forecast center (MARFC) area of forecast responsibility. The watershed is characterized by significant complexity of the bedrock geology and is a part of Susquehanna River Basin Hydrologic Observing System (www.srbhos.psu.edu).

5.1. Topographic-Geologic-Climatic Framework of Little Juniata Watershed

The topography of this region is characterized by mountains and north-east to south-west oriented valleys. There are four main streams in the watershed: Bald Eagle Creek, Spruce Creek, Sinking Valley and the Little Juniata River (see Fig. 1). The headwaters form the western boundary of the Susquehanna River Basin in this region. The Little Juniata River is the longest stream with length of 82 km. Physiographically, the watershed is within a transition zone between the Appalachian Plateau and the Ridge and Valley provinces.

Topography ranges from 204 to 800m above sea level, with the slope ranging from 0 to 55 degrees. There are significant orographic effects in the region, with precipitation determined by both orientation and altitude of the terrain [38]. Prefrontal precipitation has a critical impact on snowpack conditioning and watershed rainfall-runoff response during and after the passage of the front. Wintertime cold fronts consistently cause severe rainfall in the windward side of the orographic crest [3].

The geology of the Little Juniata watershed consists of carbonate and siliclastic mix of around ten bedrock strata including: Argillaceous limestone (ArL), Argillaceous sandstone (ArS), Calcareous shale (CSh), Dolomite (D), Limestone (L), Mudstone (M), Quartzite (Q), Sandstone (S), Shale (Sh) and Siltstone (Si). The valleys of Spruce Creek and Sinking Valley are predominantly carbonates of limestone and/or dolomite, while the higher elevations are predominantly weather-resistant siliclastic sandstones and shales. Karst valleys dominated by sinkholes and forested headwaters contribute to the importance of macropore dominated flow regimes which may also be reflected in the streamflow hydrograph response during large storms.

5.2. Distributed Data Sources

The heterogeneity in the distribution of land cover, surface and bedrock topography, hydrogeology, and atmospheric forcing, all impact the duration, timing, and dynamics of interactions among the physical processes in the watershed. The necessary data sources for PIHM simulations are listed in Table 3. Fig. 7 shows the spatial distribution of geology, soil, land cover, precipitation and elevation. The seven land cover types in this watershed are Evergreen-Needleleaf forest (Ev_NL), Deciduous Broadleaf Forest (De_BL), Mixed cover (M), Woodland (WL), Wooded Grass Land (W_GL), Crop (C) and Urban (U) with aerial coverage percentage being equal to 0.1 %, 73.8 %, 10.7 %, 3.4 %, 9.0 %, 1.9 % and 0.7 % respectively. We will show that hydrology of this bedrock aquifer system is very sensitive to the diversity in land cover and geology, with very important effects on the patterns and timing of recharge and baseflow to streams. Within the vadose zone, unsaturated hydraulic properties for porosity are derived from sand-silt-clay fraction and bulk density data obtained from the STATSGO soil database [52]. The Rosetta software [68] is used to predict hydraulic retention parameters and uncertainty range used in the Van Genuchten Eq. (11a). All types of physiographic, geologic and climate forcing distributed data and other topological relations are appropriately mapped to the model unstructured grid and discretized linear river elements in an automated way using PIHMgis [6].

6. Stream Flow and Groundwater Head Prediction Results

The model implementation is performed using a-priori parameters exclusively for soil, vegetation and other hydrogeologic properties. A limited (manual) calibration was carried out to improve the fit of model to observations. The calibration was first performed on a steady-state solution using normal (long term average) climate forcing and then the subsurface conductivity calibrated parameters obtained from it were used during the transient calibration. The steady state calibration provides a long term water balance in terms of the “normal” or long term mean conditions for precipitation and evapo-transpiration from the land surface and vegetation. The steady-state solution also is used to reduce “spin-up” time for groundwater flow, and applying the normal groundwater spatial map as the initial condition in the transient solution. The transient simulation is conducted for a period of 2 years from Nov, 1, 1983 to Oct, 31, 1985. The simulation period was selected based on the availability of the maximum number of well data (both spatial and temporal) for calibration. The average precipitation during the first year of the simulation period was 2.8 mm/d which is almost identical to the long term normal precipitation of the basin.

Model performance was initially assessed by comparing predicted ground water levels with observed values at 132 different locations (see Fig. 8). This allowed us to establish the overall scale and pattern of groundwater storage (depth to water table) in the model. Groundwater time series were only available at one location, although it was still useful for evaluating the timing of the seasonal cycle of groundwater level changes, and for event response on groundwater levels. Fig. 8 gives a comparison of the instantaneous observed and predicted ground water levels, and the location of observation wells. We note that these instantaneous observations were measured on different dates during the simulation period, and the regression pairs (observed and predicted) represent the same date. A total of 190 observations were available for the simulation period.

During the transient calibration, surface and subsurface hydrogeologic properties were modified in order to capture the time scale of the recession limb of the streamflow and groundwater hydrographs. For simplicity and tractability, uniform calibration of parameters, meaning that a parameter type was nudged by a similar percentage all over the watershed, was carried out. Fig. 9 shows the modeled and observed ground water depth time series. As stated earlier, limited calibration was performed to achieve this match. Streamflow time series were available at the watershed outlet and at one internal gauging station (see Fig. 8b). Fig. 10 shows daily observed and simulated stream outflow for the Little Juniata River and Bald Eagle Creek. The simulated streamflow (Fig. 10) was again obtained by manual adjustment of individual soil and hydrogeologic parameters over the model domain while assessing the sensitivity of local streamflow to each parameter. The model captures the event scale and seasonal streamflow response reasonably well.

The effectiveness for using a-priori data and a simple manual calibration for distributed models has also been discussed by [41]. The coefficient of determination, which explains the amount of dispersion captured by the modeled time series of the observed time series [49], for Bald Creek and Little Juniata is 0.7 and 0.74 respectively. The statistics suggest observed surface-discharge volumes and timings are reasonably captured with minimal calibration.

7. Simulating Multi-Scale, Multi-Process Behavior

The goal of this research has been to explore whether fully coupled processes and a-priori data form a practical basis for application of integrated models at the mesoscale, and to further see if this model-data coupling strategy leads to any new or interesting results that might not be obvious from weakly coupled or uncoupled approaches. Recall that our approach is based on a direct or natural coupling of the equations within a finite volume or “kernel”. We show here several examples where unexpected dynamics emerge and that the predicted phenomenon is hydraulically plausible but will require new experiments to verify. We avoid interpretation of “emergent” or self-organized behavior at this stage since most of what we observe seems to be more simply explained (i.e. principle of “lex parsimoniae”). The simulation was run on an unstructured grid generated with a minimum spatial scale of 0.048 km^2 for the watershed and 150 m for river while the minimum temporal discretization was set at 10^{-5} min. We remind the readers that depending on the dynamics of the interacting processes, the temporal discretization increases/decreases adaptively during the simulation. The spatio-temporal adaptive nature of the solution captures fine-to-large scale interactions between processes, topography and landuse/land-cover characteristics. Our focus here is on coupling behavior at event, daily, monthly and seasonal time scales. All of the presented results are for a 2 year simulation period from Nov 1983 to Oct 1985.

7.1. Interception, Evaporation, and Transpiration Dynamics

Interception, evaporation and transpiration are the primary controls on atmosphere-land surface exchange. These phenomena have been shown to be particularly critical to recycling of precipitation [26], and represent some of the most difficult and uncertain fluxes to evaluate at the watershed scale. In addition, the fully coupled model also allows us to explore how the details of land surface fluxes are related to the subsurface and stream response. In particular we are interested in land surface flux partitioning that is related to water table recharge. Using a priori data from the NLCD and spatially interpolated forcing data from NWS gauge stations and PRISM [20], PIHM simulates each flux and the results are discussed in the next 3 subsections.

7.1.1 Interception by Vegetation

As expected, the pattern of forcing (precipitation, temperature, wind speed, and net radiation) and the leaf area index (LAI) for each land cover type were found to be the first-order control on the spatio-temporal distribution of interception storage. Fig. 11a shows monthly average variations of interception for individual land cover types and for the watershed as a whole. Average interception storage for each land cover type is positively correlated with their respective Leaf Area Indices (LAIs), shown in Fig. 11b. Evergreen Needleleaf (Ev_NL) is observed to have the maximum annual average interception while agricultural crops have the minimum annual average interception of all vegetation classes. Though higher interception storage of Ev_NL is the direct consequence of its larger LAI, we note that this appears to be over-predicted by the LDAS data set [47]. Overall, the integrated model shows a strong sensitivity to the vegetation type with the cumulative annual interception storage varying from 2 mm for agricultural crops to 90 mm for Ev_NL.

7.1.2 Temporal Variation of Evaporation and Transpiration

Evaporation can occur from interception, overland flow, and the top soil layer. Transpiration varies with each land cover type and differs in terms of eco-hydrologic controls, time scales, time of occurrence, quantity and atmospheric feedbacks. Fig. 11d illustrates how monthly variation of interception loss in PIHM is largely controlled by forcing (precipitation and the seasonal energy available for evaporation, shown in Figs. 11b and 11c). In summer, average air temperature and solar radiation leads to higher interception loss, with maximum evaporation being in June. September and January demonstrate a warm and cold month with very low precipitation and low interception loss. Monthly variation of transpiration also follows a similar trend with highest and lowest values during summer and winter (October to March) respectively (see Fig. 11e). A closer look reveals an inverse relationship between the fraction of total evapotranspiration rate due to transpiration and interception loss as shown in Fig. 12a. With increasing wetted area of the plant canopy, water available for canopy evaporation increases. At the same time when interception storage increases, the leaf area that contributes to transpiration tends to decrease [67]. The inverse relationship is not valid for soil moisture, radiation and air-temperature induced limit conditions when stomatal resistance assumes extreme values. Overall, the integrated model shows a strong sensitivity to the vegetation type with the annual average ratio of P/ET_{actual} in the range of 1.75 to 2.6 from Ev_NL to agricultural crops. Evaporation from overland flow and shallow soil depth is often limited by the availability of moisture for evaporation. Since the monthly variation in precipitation pattern is not extreme and is reasonably distributed over the year, the seasonal variation in ground evaporation is largely due to incoming solar forcing as shown in Fig. 11f.

The different time scales for the evaporative flux components (interception loss, overland flow, land surface, and transpiration losses) are clearly revealed in the 2-year daily simulation. In Fig. 12b we observe that evaporation from interception in the model has both a short time scale (in response to storm events) and a seasonal time scale that modulates the interception based on seasonal temperature. We note that the model produces evaporative fluxes year round. The relative average monthly contribution of each evaporation component is shown in Fig. 12f. Transpiration dominates the total evaporative flux in summer with its contribution being as high as 54 % and then decreasing to as low as 16 % of the total in winter, with an annual mean of around 34 %. An important predicted flux in PIHM is recharge to the water table. Fig. 12e shows that most of the water available for recharge to the watershed happens during winter. The effect of this on the water availability for the remainder of the year is somewhat complex. The winter and spring recharge moves as lateral groundwater flow, supplying rates and time scale of baseflow for the rest of the season. It also contributes to evapotranspiration where shallow water table conditions provide the principal source of soil moisture and vertical upward flow. We examine the spatial implications of a shallow water table on evapotranspiration rate next.

7.1.3 Evapotranspiration Dependence on Topography and Groundwater

Spatial variations of each annual evaporative flux components predicted in PIHM are shown in Fig. 13. Fig. 13a-b shows that transpiration and interception loss closely resemble the vegetation distribution pattern (Fig. 7f). Regions with Mixed Land Cover (M) have the highest interception and transpiration loss while regions with urban landcover (U) have the smallest losses (also observed in Fig. 11). The majority of the watershed is covered by deciduous broad leaf vegetation (De_BL), which has intermediate evaporative flux values. Evaporation from ground and overland flow ($\vec{G}_7 + \vec{G}_8$) has a spatial pattern (Fig. 13c) that bears a resemblance to topography (Fig. 7e). At higher elevations, the evaporative losses from land appear to be lowest while the highest values are found at lower elevation. By plotting the evaporative flux components along an elevation transect (shown as red band in Fig. 13c) in Fig. 13e, we observe that ($\vec{G}_7 + \vec{G}_8$) have an inverse relationship to average ground water depth. Shallow water table conditions in the valleys (regions along the transect with lower elevations) result in higher evaporative losses since the capillary fringe supplies water to the unsaturated soil above the water table. The relationship is accentuated in regions of large elevation gradient. Thus topography and depth to groundwater add to the complex spatial pattern of evaporative losses which are primarily influenced by the spatial distribution of precipitation, heterogeneity of land cover/soil types and geology.

7.2. Streamflow Dynamics

Using the fully coupled formulation in PIHM, it is possible to explore a full range of river interactions with groundwater flow and overland flow. Our first finding is that the flow in a stream, the hydraulic dimensions, and the interaction of channel flow with the aquifer, apparently change at all scales within the watershed. PIHM simulations predict 7 separate fluxes for each stream reach in the model such as stream- aquifer interactions from right, left, upstream, downstream and beneath the channel and stream-overload flow interaction from right and left. To demonstrate the point at the watershed scale, the predicted mean annual streamflow distribution map for the river network in Little Juniata watershed is shown in Fig. 14(a). Expectedly, flow in the main stem (3rd order) of Little Juniata River is the largest. The average flows in 1st, 2nd and 3rd order streams are 1.35E4, 7.83E4 and 3.975E5 m^3/d respectively. In terms of the average annual flow there is a simple increase in discharge from headwater to outlet. We can also examine the annual flow-extreme maps for the network, by plotting the predicted maximum and minimum streamflow for each reach as shown in Fig. 14b and Fig. 14c respectively. There is huge seasonal variation in water availability in the stream with flow during driest periods to be only around 3 % of the flow amount during wettest periods. Overall, the predicted max, min, and mean all show a relatively smooth but decidedly different increase in flow from headwater to outlet. So one might ask the question, what are the combinations of baseflow and surface flow that produce this simple space-time pattern? Fig. 14d and 14e show the rates of base flow and overland flow per unit length for each stream reach (right+left bank) for the watershed. We note that the distribution is very heterogeneous with no simple relationship to stream order. Local examination shows that the balance of surface-subsurface contribution to the reach depends on the adjacent topography (slope, curvature, contributing area, etc.), vegetation type, and hydraulic conductivities of stream bed and the aquifer. A negative base flow is predicted in some reaches (Fig. 14d) indicating an annual loss of water to the aquifer within that reach. During drier periods, most of the stream flow (>95%) is contributed by baseflow. Fig. 14f shows the time series of the fraction of baseflow to streamflow for a yearly simulation. On an annual basis, 68% of the streamflow is contributed from baseflow.

7.3. Groundwater Recharge

Recharge, or the vertical flux of water to/from the water table is perhaps the least understood flux in a watershed. This fundamental flux is the essential component for sustaining groundwater aquifers and baseflow to streams, however it is for the most part unmeasured. The predicted recharge to the groundwater ($\vec{G}_1$) is expressed in PIHM as a complex function of both the soil moisture/pressure and the height of the water table (see Eq. 11). Fig. 15a shows the predicted spatially averaged annual recharge time series for the Little Juniata. Positive recharge denotes vertical flux from the unsaturated to the saturated zone and negative recharge represents a loss from the water table. Negative recharge denotes a combination of a) a high capillary potential in unsaturated zone due to evaporation/transpiration loss (upward flow), and b) exfiltration from shallow groundwater at the land surface. We observe that during summer (from July to October), a net negative recharge situation generally exists in the Little Juniata watershed. This implies a net flow of moisture from saturated to unsaturated zone caused by the negative potential created by evaporative and transpirative loss from shallow water table zones, seepage zones or wetlands. We also note that recharge events are rapidly varying in summer (changing signs from positive to negative within short time intervals) as opposed to winter (positive only). The slow variation in winter is because of the lower conductivity of frozen top soil layer which reduces the infiltration rate. The spatial distribution of recharge is found to be closely related to land cover type, hydraulic conductivity of the soil surface and geology, and topography. Fig. 15b illustrates a large positive groundwater annual recharge component near the streams and adjacent valleys. At the higher elevations, net annual recharge is much smaller. Although we have limited data to verify the simulated results, the valley soils seem to have a strong macropore effect on recharge which is enhanced by overland flow from adjacent steeper terrain. It may also be that the valley limestone-derived soils tend to maintain water in the soil matrix more efficiently than upland soils (of finer grain size). Recall that macropore flow in PIHM is initiated when the soil matrix is near saturation or when overland flow is occurring.

7.4. Streamflow-Groundwater Dynamics and Local Topographic Control

An important aspect of fully coupled processes in PIHM is the ability to examine details of exchanging water along the river or riparian corridor. For the Little Juniata we find that the simulated exchange of water between the channel and the local groundwater is quite complex and that a simple classification of gaining and losing channel reaches does not quite describe the dynamics over all time scales. We find that the classical flow exchange of groundwater and surface water is better described in terms of the relative frequency of gaining or losing channels. The 3 conditions are: a) a *predominantly losing* reach (loses flow >90% of the time), b) a *predominantly gaining* reach (gains water >90% of the time), and c) an *intermittent gaining/losing* reach. Fig. 16a shows the distribution of the fraction of time over the 2 year simulation that each stream section gains water as base flow. We note that one minus the fraction of time the stream is gaining water represents the frequency of losing or non-gaining. In the Little Juniata watershed there is a large streamflow contribution from the baseflow, because of macropores and localized highly permeable (karst) geology, resulting in most of the stream sections being predominantly gaining for most of the year. On the average a typical stream section in the watershed is gaining 88% of the time during the 2 year simulation period. 1st order, 2nd order and 3rd order streams are observed to be gaining for increasingly larger times varying from 78% to 93% to 98% respectively. However, there are many reaches where predominantly losing flow is predicted by the model.

Fig. 16b-d shows the baseflow hydrograph for the simulation period for three cases discussed above. Note that baseflow hydrographs are predicted independently for each side of a channel reach. This is important particularly in cases where there is a marked difference in groundwater head of the aquifer on the either side of the channel. This results in negative baseflow contribution to one side of the aquifer and positive base flow contribution to the opposite. Such a channel is referred to here as a "flow-through" channel. Occurrence of "flow-through" channels generally occurs where there is a sharp topographic change on opposite sides of the stream, or there exists a shallow impermeable rock layer on one side of the channel, or a high permeability zone on one side of the channel. Fig. 16c shows an intermittently gaining reach which also happens to be "flow through channel" section. During wet seasons, the stream receives base flow from one side but then recharges the aquifer on the other side at higher rate due to local hydraulic gradients. During relatively dry periods "flow through" behavior of the reach continues, but the river experiences a net gain of water. During and shortly after large storm events, Fig. 16c shows that the river loses water through bank infiltration, thus reducing the flood level and recharging the aquifer. The volume of this *bank recharge* depends on duration, height, and shape of the flood hydrograph, as well as on the transmissivity and storage capacity of the aquifer and the permeability of the stream sediments. This successive discharge and recharge of the aquifer has a buffering effect on the runoff regimes of rivers [13] and is likely a critical but unresolved element in stream-aquifer contamination. Overall, the intermittent gaining/losing behavior is common in many flow-through reaches in this watershed. Fig. 16d illustrates a predominantly losing stream. We note that such streams are more likely to exist on relatively steep hillslopes where groundwater level is always below the stream bed. These streams are often ephemeral with significant flow only during storm events. Fig. 16d shows the baseflow hydrograph in response to precipitation events, and that the stream reach loses flow 98% of the time.

Fig. 17 illustrates the effects of stream morphology and stream order on the surface-groundwater exchange. The example shows how predominantly gaining tributaries can switch regime at the confluence with higher order channels. A conceptual model for this change in regime seems to depend on the seasonal conditions as illustrated in Fig. 17. During the wet or high runoff season, both the tributary and the higher order channel are gaining flow. However in the dry season, lower ground water table conditions lead to the tributary outlet switching to a losing channel. Thus it can be concluded that the distribution of predominantly gaining or losing and intermittent streams are highly influenced by the seasonal groundwater conditions and the local physiography [82]. This condition is also likely to be related to the timing, intensity and pattern of precipitation within each tributary in addition to the effects of landscape morphology.

7.5. Seasonal Event-Based Coupled Dynamics

Next we examine the impact of forcing and land interactions on the magnitude of runoff in different seasons. Fig. 18a-b illustrates two storm events (also identified in Fig. 10) averaged for the entire watershed area, each of 10 days duration and with very similar intensity. The runoff hydrographs are for the watershed outlet. Event 1 takes place in winter (February) while Event 2 takes place in summer (June). The total amount of precipitation in summer event is in fact larger (9.4 cm) than the winter 1 (7.7 cm), although the streamflow generated for summer storm is much less. This difference in watershed response can be explained by the partitioning of precipitation (see Fig. 18c-h) as it interacts with vegetation (interception loss) and ground (evapotranspiration). Dense summer vegetation with large LAI, produces much greater interception storage (~ 0.199 mm) in the summer. We also note that the higher summer temperature results in larger interception loss thus reducing the throughfall contribution to overland flow and groundwater recharge. Infiltration loss during the summer event is also larger due to the larger seasonal soil moisture deficit and generally lower water table. All this results in a net smaller contribution of baseflow (see Fig. 18g-h) and overland flow (see Fig. 18e-f) to the streamflow in summer, inspite of larger intensity storms. Overall, evapotranspiration, interception storage and initial watershed state play a crucial role in determining overland and subsurface flow response.

8. Conclusions

This paper presents the coupling strategy and a mesoscale application of the PIHM model. A range of issues that arise from the coupling of data, process and numerical solution are discussed. We note that the strategy for unstructured mesh decomposition, the local definition of kernel (system of equations), and use of an advanced implicit solver are critical elements of accurate and efficient modeling. We use an adaptive discretization methodology to resolve the necessary spatial scales in PIHM. By applying the model to simulate a mesoscale river basin, the Little Juniata watershed, we show how stream-aquifer interactions are a function of local topography, land cover, geology and soil type. Although there are many variables at work, the a-priori parameters used in PIHM, and the natural coupling of the equations lead to very plausible explanations and several useful predictions of the hydrologic, climatic and ecological conditions that exist in the Little Juniata throughout the water year. The time scales of process interactions are found to vary spatially and temporally. Evapotranspiration, and particularly interception loss is shown to play a crucial role in determining overland and subsurface flow response. Limited observed data for groundwater, and streamflow still allowed us to make an initial validation of the watershed dynamics and to make qualitative predictions for internal fluxes between all states in the watershed. New predictions in terms of distributed spatio-temporal stream-aquifer interaction (gaining/loosing streams) maps, groundwater recharge maps, distributed stream flow maps and process separation at multiple scales is obtained. We attempt to make a case for the importance of an integrated modeling framework, which in the future will also require a new kind of observing system that can resolve and test the coupled dynamic predictions beyond the a-priori data used here. The integrated theory provides a new way to "explore" hydrologic states and can be used to develop scenarios of change for parameters, forcing data sets, and new descriptions of the physical processes. The success of this fully-coupled model in predicting the stream flow hydrographs at the outlet and internal points in a basin of this size (~900 sq. km) while also capturing process interactions within in the watershed at adaptively fine time scales lends credence to the potential of using fully coupled distributed hydrologic models for operational forecasting, water management, as well as a research and analysis tool to answer and unravel science questions.

References

[1] Abbott MB, Bathurst JC, Cunge JA, O'Connell PE, Rasmussen J. An Introduction to the European Hydrological System – Systeme Hydrologique Europeen, "SHE", 2 : History and Philosophy of a Physically-based, Distributed Modelling System. Journal of Hydrology, 87, 61-77; 1986.

[2] Anderson S, Dietrich W, Montgomery D, Torres R, Conrad M, Loague K. Subsurface flow paths in a steep, unchanneled catchment. Water Resources Research 33(12); 1997.

[3] Barros AP, Kuligowski RJ. Orographic Effects During a Severe Wintertime Rainstorm in the Appalachian Mountains. Monthly Weather Review, 126, 2648-2672; 1998

[4] Beven K, Germann PF. Macropores and water flow in soils. Water Resources Res. 18 (5). 131 1-1325; 1982

[5] Beven KJ. Distributed models, in M.G. Anderson and T.P. Burt (Eds) Hydrological forecasting, Wiley, Chichester; 1985

[6] Bhatt G, Kumar M, and Duffy CJ. Bridging the gap between geohydrologic data and distributed hydrologic modeling. In Proceedings of International Congress on Environmental Modeling and Software; 2008

[7] Blayo E, Debreu L. Adaptive mesh refinement for finite-difference ocean models: first experiments. J. Phys. Ocean., 29 (6), 1239-1250; 1999

[8] Blondin C. Parameterization of land-surface processes in numerical weather prediction, in Land Surface Evaporation; Measurements and Paramrleizuliun, edited by T.J. Schmugge and J.C. Andre, pp. 31-54, Springer-Vedag, New York; 1991

[9] Bosch JM, Hewlett JD. A review of catchment experiments to determine the effect of vegetation changes on water yield and evapotranspiration. J. Hydrol., 55, 3-23; 1982

[10] Bougeault P. Parameterization schemes of Land-Surface processes for mesoscale Atmospheric models. In Land Surface Evaporation, edited by T. J. Schmugge and J. Andre´ (New York: Springer-Verlag), pp. 55–92; 1991

[11] Brooks RH, Corey AT. Hydraulic properties of porous media, Hydraulic Paper #3. Colorado State University, Ft. Collins, CO; 1964

[12] Brown DL. An analysis of transient flow in upland watersheds: interactions between structure and process Ph.D. dissertation, University of California, Berkeley, California; 1995

[13] Brunke M, Gonser T. The ecological significance of exchange processes between rivers and ground-water. FreshwaterBiol 37:1–33; 1997

[14] Byrne GD. Pragmatic experiments with Krylov methods in the stiff ODE setting. In Computational Ordinary Differential Equations, J. Cash and I. Gladwell, Eds. Oxford University Press, Oxford, U.K., 323-356; 1992

[15] Chen ZT, Guevara JA. Systematic selection of very important points (VIP) from digital terrain models for constructing triangular irregular networks. Proceedings, AUTO-CART0 8, Baltimore 1987, pp. 50-56; 1987

[16] Chen C, Wagenet RJ. Simulation of water and chemicals in macropore soils. Journal of Hydrology 130, 105-149; 1992

[17] Cohen SD Hindmarsh AC. CVODE user guide. Technical report UCRL-MA-118618, Lawrence Livermore National Laboratory; 1994

[18] Courant R, Friedrichs K, Lewy H. Uber die partiellin differenzengle-ichungen der mathematischen physik. Math Ann;110:32-74; 1928

[19] Daly C, Neilson RP, Phillips DL. A statistical-topographic model for mapping climatological precipitation over mountainous terrain, J. Appl. Meteorol, 33, 140-158; 1994

[20] Daly C, Taylor GH, and Gibson WP. The PRISM approach to mapping precipitation and temperature, paper presented at 10th Conference on Applied Climatology, Am. Meteorol. Soc., Reno, Nev., Oct. 20-24, 1997

[21] Deardorff JW. Efficient prediction of ground surface temperature and moisture, with inclusion of layer of vegetation. Journal of Geophysical Research, 83, 1889–1903; 1978

[22] Dickinson RE. Modelling evapotranspiration for three-dimensional global climate models. In Climate Processes and Climate Sensitivity, Geophysical Monograph Service, 29, edited by J. E. Hansen and T. Takahashi, AGU (Washington, DC: AGU), pp. 58–72; 1984

[23] Di Giamarco, Todini PE, and Lamberti P. A conservative finite elements approach to overland flow: the control volume finite element formulation. J. Hydrol., 175 pp.267-291; 1996

[24] Dingman SL. Physical Hydrology, Macmillan, pp. 370-373; 2002

[25] Duffy CJ. Semi-Discrete Dynamical Model for Mountain-Front Recharge amd Water Balance Estiamation. In: Groundwater Recharge in a Deseart Environment: The

Southwestern US, Editos: J. Hogan, F. Phillips, B. Scanlon, Water Science and Application Monograph, American Geophysicsl Union. Pp.236-255; 2004

[26] Eltahir EAB, Bras RL. Precipitation recycling in the Amazon basin. Quarterly Journal of the Royal Meteorological Society 120: 861–880; 1994

[27] Fairbanks J, Panday S, Huyakorn PS. Comparisons of linked and fully coupled approaches to simulating conjunctive surface/ subsurface flow and their interactions. In: Seo, Poeter, Zheng, Poeter, editors. MODFLOW 2001 and Other Modeling Odysseys— Conference Proceedings, Golden, CO;p. 356–61; 2001

[28] Feng K, Molz FJ. A 2-D, diffusion-based, wetland flow model. Hydrol., 196: 230-250; 1997

[29] Freeze RA. Mathematical Models of Hillslope hydrology, in M.J. Kirkby (ed), Hillslope Hydrology, Wiley, New York, pp. 177-225; 1978

[30] Gerke HH, van Genuchten MT. A dual-porosity model for simulating the preferental movement of water and solutes in structured porous media. Water Resour. Res. 29,305–319; 1993

[31] Gottardi G, Venutelli M. A control-volume finite-element model for two-dimensional overland flow. Adv Water Resour ;16:277–84; 1993

[32] Govindaraju RS, Kavvas ML. Dynamics of moving boundary overland flows over infiltrating surfaces at hillslopes. Water Resour Res;27(8):1885–98; 1991

[33] Graham DN and Refsgaard A. MIKE SHE: a distributed, physically based modeling system for surface water/groundwater interactions. In: Seo, Poeter, Zheng, Poeter, editors. MODFLOW 2001 and Other Modeling Odysseys—Conference Proceedings, Golden, CO; p. 321–7; 2001

[34] Herdendorf CE. Morphometric Factors in the Formation of Great Lakes Coastal Wetlands. Aquatic Ecosystem Health and Management 7(2):179−197; 2004

[35] Hernandez M, Miller SN, Goodrich DC, Goff BF, Kepner WG, Edmonds CM, Jones KB. Modeling Runoff Response to Land Cover and Rainfall Spatial Variability in Semi-arid Watersheds. Journal of Environmental Monitoring and Assessment, 64: 285-298. Kluwer Academic Publishers; 2000

[36] Hoogmoed WD, Bouma J. A simulation model for predicting infiltration into cracked clay soil. Soil Sci.Soc. Am. J. 44:458-461; 1980

[37] Hornbeck JW, Pierce RS, Federer CA. Streamflow changes after forest clearing in New England. Water Resour. Res., 6, 1124-1132; 1970

[38] Hosler CL, Davis LG, Booker DR. Modification of convective systems by terrain with local relief of several hundred meters. Z. Angew. Math. Phys., 14, 410–418; 1963

[39] Hutson JL, Wagenet RJ. A multiregion model describing water flow and solute transport in heterogeneous soils. Soil Sci.Soc. Am. J. 59, 743–751; 1975

[40] Huyakorn PS, Springer EP, Guvanasen V, Wadsworth TD, A three dimensional finite element model for simulating water flow in variably saturated porous media. Water Resour Res;22(12):1790–808; 1986

[41] Ivanov VY, Vivoni ER, Bras RL, Entekhabi D. Catchment hydrologic response with a fully distributed triangulated irregular network model, Water Resourc Res., Vol. 40; 2004

[42] Jarvis PG, The interpretations in the variations in leaf water potential and stomatal conductance found in canopies in the field. Philos Trans R Soc London, Ser B 273: 593–610; 1976

[43] Jenny H. Factors of Soil Formation; A system of quantitative pedology: New York, Dover Publications, Inc., 281 p.; 1994

[44] Jones JE, Woodward CS. Preconditioning Newton–Krylov methods for variable saturated flow. In: Bentley LR, Sykes JF, Brebbia CA, Gray WG, Pinder GF, editors. Computational methods in water resources, Vol. 1. Rotterdam: Balkema; 2000. p. 101–6; 2000

[45] Jones JE, Woodward CS. Newton–Krylov-multigrid solvers for large-scale, highly heterogeneous, variably saturated flow problems. Adv Water Resour 2001;24:763–74; 2001

[46] Langevin C, Swain E, Wolfert M. Simulation of Integrated Surface-Water/Ground-Water Flow and Salinity for a Coastal Wetland and Adjacent Estuary. Journal of Hydrology 314 (1-4), 212-234; 2005

[47] LDAS, Acessed Apr. http://ldas.gsfc.nasa.gov/LDAS8th/EROSveg2/LDASvegetation2.shtml; 2007

[48] Kollet SJ, Maxwell RM. Integrated surface-groundwater flow modeling: A free-surface overland flow boundary condition in a parallel groundwater flow model, Advances in Water Resources, (29)7, 945-958; 2006.

[49] Krause P, Boyle DP, Base F. Comparison of different efficiency criteria for hydrological model assessment, Advances in Geosciences, Vol. 5, pp 89-97, 16-12-2005; 2005

[50] Kumar M, Bhatt G, Duffy CJ. An efficient domain decomposition framework for accurate representation of geodata in distributed hydrologic models, International Journal of GIS; 2008

[51] Kumar M, Bhatt G, Duffy CJ. Shared data model to support sensor network data in hydrologic models. In Proceedings of International Congress on Environmental Modeling and Software; 2008

[52] Miller DA, White RA. A conterminous United States multi-layer soil characteristics data set for regional climate and hydrology modeling, Earth Interactions 2, (available at http://EarthInteractions.org); 1998

[53] Mohanty BP, Bowman SR, Hendrickx JMH, van Genuchten MT. New piecewise-continuous hydraulic functions for modeling preferential flow in an intermittent-flood-irrigated field. Water Resour. Res. 33, 2049–2073; 1997

[54] Morse PM, Feshbach H. Methods of Theoretical Physics, Part I. New York: McGraw-Hill, p. 657; 1953

[55] Mosley MP, Subsurface How velocities through selected forest soils, South Island, New Zealand, J. Hydrol. 55, 65-92; 1982

[56] Nanson GC. Point bar and floodplain formation of the meandering Beatton River, northeastern British Columbia, Canada Sedimentology 27 (1), 3–29; 1980

[57] Pan D, Cheng JC. Upwind Finite-Volume Navier Stokes Computations on Unstructured Triangular Meshes, AIAA Journal, Vol 3, 9; 1993

[58] Panday S, Huyakorn PS. A fully coupled physically-based spatially-distributed model for evaluating surface/subsurface flow. Adv Water Resour 27:361–382; 2004

[59] Paniconi C, Wood EF. A detailed model for simulation of catchment scale subsurface flow processes, Water Resour. Res., 29(6), 1601-1620; 1993

[60] Perillo GME, Minkoff DR, Piccolo MC. Novel mechanism of stream formation in coastal wetlands by crab–fish–groundwater interaction, Earth and Environmental Science, Vol. 25, 4; 2005

[61] Qu Y, Duffy CJ. A semi-discrete finite volume formulation for multi-process watershed simulatioin, Water Resourc. Res; 2007

[62] Richards LA. Capillary conduction of liquids in porous mediums. Physics 1:318–333; 1931

[63] Refsgaard J, Storm B. MIKE SHE, pp 809-846 in Computer Models for Watershed Hydrology, Water Resource Public., Fort Collins, Colorado; 1996

[64] Rushton KR, Tomlinson LM. Possible mechanisms for leakage between aquifers and rivers. J Hydrol 40:49–65; 1979

[65] Roberson JA, Crowe CT. Engineering fluid mechanics. third ed. Boston: Houghton Mifflin Company; 1985; 1985

[66] Rutter AJ, Morton AJ. A predictive model of rainfall interception in forests, 111. Sensitivity of the model to stand parameters and meteorological variables. J. Appl. Ecol. 14:567-588; 1977

[67] Savenije HHG. The importance of interception and why we should delete the term evapotranspiration from our vocabulary. Hydrological Processes, 18(8):1507-1511; 2004

[68] Schaap MG, Leij FJ. Database Related Accuracy and Uncertainty of Pedotransfer Functions, Soil Science 163:765-779; 1998

[69] Schmidt M, Kerschgens M, Hübener H, Sogalla M. Simulating evapotranspiration in a semi-arid environment, Theoretical and Applied Climatology, (Vol. 80) (No. 2/4) 153-167; 2005

[70] Shuttleworth WJ Evaporation. Chapter 4. In Handbook of Hydrology, Maidment DR. McGraw-Hill: New York, USA; 1993

[71] Srivastava R, Yeh T. Analytical solutions for one-dimensional, transient infiltration toward the water table in homogeneous and layered soils. Water Resources Research 27(5); 1991

[72] Strelkoff T. Numerical solution of Saint Venant equations. ASCE Proceedings, Journal of Hydraulic Dicision 96: 223-252; 1970

[73] Tóth J. A conceptual model of the groundwater regime and the hydrogeologic environment. J Hydrol 10:164–176; 1970

[74] USACE. Snow Hydrology, Summary report of the Snow Investigations, U.S. Army Corps of Engineers, North Pacific Division, Portland, Oregon; 1956

[75] USACE UNET. One-dimensional unsteady flow through a full network of open channels, User's Manual. US Army Corps of Engineers, Hydrologic Engineering Center, Davis, CA; 1997

[76] Valorani M, Goussis DA. Explicit Time-Scale Splitting Algorithm for Stiff Problems: Auto-ignition of Gaseous Mixtures behind a Steady Shock. Journal of Computational Physics, 169, 44-79; 2001

[77] VanderKwaak JE. Numerical simulation of flow and chemical transport in integrated surface–subsurface hydrologic systems, Doctorate Thesis, Department of Earth Sciences, University of Waterloo, Ontario, Canada; 1999

[78] van Genuchten, MT. A closed-form equation for predicting the hydraulic conductivity of unsaturated soils. Soil. Sci. Soc of Am. J. 44, 892–898; 1980

[79] Vivoni ER, Ivanov VY, Bras RL, Entekhabi D. Generation of triangulated irregular networks based on hydrological similarity, Journal of hydrologic engineering, 9, 4. 288-302; 2004

[80] Whipkey RZ, Kirkby MJ. Flow within the soil. In Hillslope Hydrology, Kirkby MJ (ed.). Wiley: Chichester; 121–144; 1978

[81] Winter TC. Relation of streams, lakes and wetlands to groundwater flow systems, Hydrogeology Journal 7, 28-45; 1999

[82] Woessner WW. Stream and fluvial plain ground water interactions: rescaling hydrogeologic thought. Ground Water 38(3): 423–429; 2000

[83] Yeh GT, Huang GB. A Numerical Model to Simulate Water Flow in Watershed Systems of 1-D Stream-River Network, 2-D Overland Regime, and 3-D Subsurface Media (WASH123D: Version 1.5), Technical Report. Dept. of Civil and Environmental Engineering, University of Central Florida, Orlando, Florida; 2003

Appendix

Appendix I

β Percentage area fraction of macropore

C_d Coefficient of discharge (Dimensionless)

C_{pa} Specific heat capacity of air at constant pressure ($L^2T^{-2}\theta^{-1}$)

Δ Slope of saturation vapor pressure curve ($MLT^{-2}\theta^{-1}$)

e_j Width of a triangular edge

$(e_{sz} - e_z)$ Vapor pressure deficit ($ML^{-1}T^{-2}$)

f_s Snow Fraction

$vFrac$ Fractional areal vegetation cover

$\vec{F}_0$ Lateral surface flux exchange (LT^{-1})

$\|\vec{F}_1\|$ Lateral surface flux exchange between overland flow and channel (LT^{-1})

$\vec{F}_2$ Lateral groundwater flux exchange (LT^{-1})

$\|\vec{F}_3\|$ Lateral flux exchange between channel and ground water (LT^{-1})

$\|\vec{F}_4\|$ Later groundwater flux exchange between sub-channel and triangular watershed element (LT^{-1})

$\vec{F}_5$ Flux exchange between river segments (LT^{-1})

γ Psychometric constant ($ML^{-1}T^{-2}\theta^{-1}$)

g Acceleration due to gravity (LT^{-2})

$\vec{G}_0$ Infiltration/Exfiltration rate (LT^{-1})

$\vec{G}_1$ Recharge flux between unsaturate zone and ground water (LT^{-1})

$\vec{G}_2$ Vertical flux exchange between channel bed and ground water (LT^{-1})

$\vec{G}_3$ Net precipitation flux to the canopy/ground/river (LT^{-1})

$\vec{G}_4$ Evaporation from canopy (LT^{-1})

$\vec{G}_5$ Throughfall drainage (LT^{-1})

$\vec{G}_6$ Snow melt (LT^{-1})

$\vec{G}_7$ Evaporation from overland flow (LT^{-1})

$\vec{G}_8$ Evaporation from upper soil layer (LT^{-1})

$\vec{G}_9$ Transpiration (LT^{-1})

K_{eff} Effective conductivity (arithmetic/harmonic mean of the neighboring conductivities

K_{eq} Equivalent hydraulic conductivity of dual matrix-macropore system

$K_{macV}[S]$ Vertical macropore hydraulic conductivity

$K_{macH}[S]$	Horizontal macropore hydraulic conductivity
$K_{\max}$	Maximum hydraulic conductivity of dual matrix-macropore system
$K_{matV}[S]$	Vertical matrix hydraulic conductivity at saturation S
$K_{matH}[S]$	Horizontal matrix hydraulic conductivity at saturation S
K_u	Vertical conductivity of the unsaturated zone
L_j	Length of a channel segment
n_s	Manning's coefficient ($L^{-1/3}T$)
Q^*	Net radiation (MT^{-3})
r_a	Atmospheric diffusion resistance (TL^{-1})
S	Saturation of the unsaturated zone
S_1	Sink flux from ground water (LT^{-1})
Sf	Surface Overland Flow (LT^{-1})
Sf_r	Surface Flow from Land to River(LT^{-1})
T_a	Air Temperature (T)
T_b	Base Temperature (T)
$vFrac$	Vegetation Fraction (Dimensionless)
z_r	River bed elevation (L)
z_{rb}	River bank elevation (L)
z_b	Aquifer bed elevation (L)
z_i	Surface elevation at i^{th} control volume

Appendix II

$$grad\psi\big|_x = \frac{y_2(z_1 - z_0) + y_1(z_0 - z_2) + y_0(z_2 - z_1)}{x_2(y_0 - y_1) + x_0(y_1 - y_2) + x_1(y_2 - y_0)}$$

$$grad\psi\big|_y = \frac{x_2(z_1 - z_0) + x_1(z_0 - z_2) + x_0(z_2 - z_1)}{y_2(x_0 - x_1) + y_0(x_1 - x_2) + y_1(x_2 - x_0)}$$

$$grad\psi = \sqrt{(grad\psi\big|_y)^2 + (grad\psi\big|_x)^2}$$

where x_i, y_i and z_i are coordinates of neighboring cell centers and $z_i = z + \psi$

Appendix III

Using Richard's equation and mass balance at the unsaturated-saturated zone interface as shown in Fig. 19 we get

$$\vec{G}_1 = K_u \frac{\psi_u - \psi_{us}}{0.5(z - z_b - \psi_4)} = K_s \frac{\psi_{us} - (z_b + \psi_4)}{0.5\psi_4}$$

$$\psi_{us} = \frac{2K_u K_s (\psi_u - (\psi_4 + z_b))}{K_s(z - z_b - \psi_4) + K_u \psi_4}$$

$\Rightarrow$

Replacing ψ_{us} in the expression for $\vec{G}_1$ and using van-Genuchten's $\psi - S$ relationship (Eq. 11a) in the unsaturated zone we get equation 11

$$G_1 = \frac{K_u K_s z_b (\alpha(z - z_b - \psi_4) - 2(-1 + S^{\frac{n}{1-n}})^{\frac{1}{n}})}{\alpha(K_u \psi_4 + K_s(z - z_b - \psi_4))}$$

Appendix IV

A representative non-linear "stiff" ODE system with a combination of faster and smaller time scales is

$$\frac{dy}{dt} = g(y), \qquad y(0) = y_0 \tag{24a}$$

where y and g are N dimensional state and functional vectors respectively. The right hand side of the above equation can be linearized to obtain

$$\frac{dy}{dt} = g(y) = \frac{dg_i}{dy_j} y_i = JY = (A\lambda B)Y$$

An example of one such stiff ODE system defined on a PIHM kernel is an interaction between overland and ground water flow processes. Assuming a shallow groundwater condition with direct interaction between surface and ground water, Eq. (24b) shows a simplified representation of process interactions on a model kernel i that neighbors j (in accordance with Eq. 5) using a 2-dimesional stiff ODE system with state vector $y \equiv (\psi_2, \psi_4)$.

$$\begin{pmatrix} \dfrac{d\psi_2}{dt} = S_0 - (S_4 + S_5) - \dfrac{1}{n}\psi_{2i}{}^{5/3} \dfrac{\psi_{2i} - \psi_{2j} + (z_i - z_j)}{d} \dfrac{L}{A} - K_v \dfrac{\psi_{2i} - \psi_{3i} + (z_i - z_{u_i})}{(z_i - 0.5 z_{u_i})} \\ \dfrac{d\psi_4}{dt} = K_v \dfrac{\psi_{2i} - \psi_{3i} + (z_i - z_{u_i})}{(z_i - 0.5 * z_{u_i})} - K_h \dfrac{\psi_{4i} - \psi_{4j} + (z_{bi} - z_{bj})}{d} \psi_{4ij} \dfrac{L}{A} \end{pmatrix}$$

(24b)

The eigenvalue of the jacobian for ODE system in (24b) will be

$$\begin{pmatrix} \lambda_1 \\ \ldots\ldots \\ \lambda_2 \end{pmatrix} = \begin{pmatrix} (-\frac{1}{n}\psi_{2i}{}^{5/3} \dfrac{(1+\frac{5}{3}\dfrac{\psi_{2i}-\psi_{2j}+(z_i-z_j)}{\psi_{2i}}}{dA} L - \dfrac{K_v}{(z_i-0.5z_{u_i})} \\ \ldots\ldots\ldots\ldots\ldots\ldots\ldots\ldots\ldots\ldots\ldots\ldots \\ -\dfrac{K_h(\psi_{4ij}+(\psi_{4i}-\psi_{4j}+(z_i-z_j))/2)}{dA} L \end{pmatrix}$$

We note that with typical values of the states and roughness and conductivity parameters in (24b), the ratio $\lambda_1/\lambda_2 \approx \dfrac{\psi_2{}^{5/3}}{n\psi_4 K_h}$ means $\lambda_1 > \lambda_2$. In the same vein, assuming that M eigenvalues of the total N for the global ODE system (shown in Eq. 24a) are very large, the exact solution obtained from a first order explicit method [76] can be written as

$$y_{ex}(t) = (\sum_{i=1}^{M} a_i e^{\frac{\ln|1-\lambda_i \Delta t|}{\Delta t}t} e^{\frac{i\pi t}{\Delta t}} b_i + \sum_{i=M+1}^{N} a_i e^{\frac{\ln|1-\lambda_i \Delta t|}{\Delta t}t} e^{\frac{i\pi t}{\Delta t}} b_i) y_0 \tag{24c}$$

where $y_{ex}(t)$ is the explicit solution. For the explicit solution to be stable, the following conditions need to be satisfied.

$$\forall i \qquad \ln|(1-\lambda_i\Delta t)| <= 0 \;\; \Rightarrow \;\; |1-\lambda_i \Delta t| <= 1 \;\; \Rightarrow \;\; \Delta t \le 1/|\lambda_i|$$

Since $|\lambda_1| > |\lambda_2| > |\lambda_3| > \ldots\ldots |\lambda_M| >> |\lambda_{M+1}| > \ldots\ldots\ldots\ldots |\lambda_N|$, the stability of the explicit system will require $\Delta t \le 1/|\lambda_1|$. For a stiff system with very large λ_1, Δt will be very small. We note that these stability requirements are in addition to the CFL stability condition [18] which depends on grid size, Courant number, velocity and depth of flow in other similar flow systems. On the contrary, the implicit solution [76] given by

$$y_{im}(t) = (\sum_{i=1}^{M} a_i e^{\frac{-\ln(1+\lambda_i \Delta t)}{\Delta t}t} b_i + \sum_{i=M+1}^{N} a_i e^{\frac{-\ln(1+\lambda_i \Delta t)}{\Delta t}t} b_i) y_0 \tag{24d}$$

is always stable for all $\lambda_i \Delta t > 0$.

Figures

Fig. 1. Unstructured domain decomposition of Little Juniata Watershed generated with (right) and without (left) the use of subwatershed boundaries and streamflow observation station as constraints. Note that in decomposition with the constraints, the observation station acts as a node of the river discretization element (right). The modeled flux location will be exactly at the gauge location thus appropriately accounting for the exact contributing area. Also the mesh boundary coincides with subwatershed boundaries (right) thus preserving necessary surface water flow directions.

Fig. 2. Prismatic (top left) and linear River (top right) kernels constitute a model domain. We note that each linear river kernel is sandwiched between neighboring watershed prismatic kernel elements. A kernel is a stack of control volumes corresponding to different states. Process interactions across the control volumes faces (listed in Table 1) are also shown. Sub-paneled graphics correspond to control volumes for a) Vegetation b) Overland Flow c) Unsaturated Zone d) Saturated Zone e) River flow and f) Groundwater flow below river bed.

Fig. 3. Groundwater flux across all the three prismatic kernel edges depends on the head gradient across it

Fig. 4. $\nabla_s \psi$ for the unit element *i* in Eq. (13) is calculated by approximating a triangular stencil over neighboring elements. The graphic on the right addresses the case when a prismatic element neighbors a river. The expression for the gradient is in Appendix II.

Fig. 5. Two cases of surface flow across the "weir/dam" type channel bank. Case on the left pertains to when river stage is lower than the river bank height while case on the right has river stage larger than the bank height. We note that for the both cases shown above, $(\psi + z)_u$ in Eq. (15) will be (z+ψ_2)

Fig. 6. Graphic on the left shows how PIHM defines the depth of macropores (*macD*). The surface "skin-depth" *2d* is defined as the depth over which the infiltration is calculated. The conceptual model of infiltration/exfiltration based flow is shown in the right graphic where the system is divided into a dual matrix with micropore and macropore media

Fig. 7. Distributed data map of a) Precipitation (Nov, 1983) b) Temperature (Nov, 1983) c) Soils d) Geology e) Elevation and f) Land Cover for Little Juniata Watershed. Data sources are listed in Table 3.

Fig. 8. Modeled groundwater head (MGwH) vs. Observed groundwater head (OGwH) for the observation wells (shown in the lower graphic) for the 1983 -84 period of the model run. Data source for observed head: http://nwis.waterdata.usgs.gov/nwis/gw

Fig. 9. Modeled and Observed ground water depth time series. Data source for observed head: http://nwis.waterdata.usgs.gov/nwis/gw

Fig. 10. Observed and Modeled Streamflow at a) Little Juniata River Observation Station b) Bald Eagle Creek Observation station. Data source for observed head: http://nwis.waterdata.usgs.gov/nwis/sw

Fig. 11. a) Average monthly interception storage for different land cover types. Expectedly, variation in interception storage is correlated with precipitation. b) Variation of monthly precipitation and LAI. c) Monthly average of incoming solar radiation d) Monthly aveage of evaporation from interception storage ($\vec{G}_4$) shows signatures of its dependence on interception storage (maximum in August) and Incoming solar radiation (maximum in June e) Temporal variation in monthly transpiration ($\vec{G}_9$) has a strong dependence on LAI and radiation. f) Monthly evaporation from overland flow and the upper soil layer ($\vec{G}_7 + \vec{G}_8$) is found to follow annual cycle of temperature and radiation

Fig 12: a) Variation of fractional loss components (transpiration and interception loss) with respect to total evapotranspiration. We note that when fraction of transpiration to total evapo-transpiration increases, the corresponding fraction of interception loss decreases and vice-versa. b) Annual variation of daily interception loss rate, $\vec{G}_4$ (Annual average $\vec{G}_4$ = 0.000288 m/d) c) Annual variation of daily transpiration loss rate, $\vec{G}_9$ (Annual average $\vec{G}_9$ = 0.000466 m/d) d) Annual variation of daily evaporation rate from ground, $\vec{G}_7 + \vec{G}_8$ (Annual average $\vec{G}_7 + \vec{G}_8$ = 0.000387 m/d). e) Average monthly precipitation and evapotranspirative loss f) Relative percentage contribution of each evapo-transpirative flux component

Fig. 13. Spatial pattern of annual average evaporation from a) canopy and b) transpiration closely reflect the vegetation pattern. (shown in (d)). Spatial pattern of ground evaporation (shown in (c)) strongly depends on the depth of ground water and recharge pattern. Figure (e) shows that the variation of evaporation from ground ($\vec{G}_7 + \vec{G}_8$) along a transect across the valley (shown as a rectangular strip in (c)) follows an inverse relationship to ground water depth (and elevation). $\vec{G}_7 + \vec{G}_8$ are larger where there are shallow groundwater conditions (at lower elevations) and vice-versa.

Fig. 14. (a) Spatial distribution of annual average flow in the stream network of Little Juniata Watershed. b) Maximum and c) minimum flow in each section of river. d) Baseflow (BF) and e) overland flow (OLF) contribution to river per unit length of stream varies heterogeneously depending on local topography and hydrogeologic properties. f) Base flow contribution (BF) to total streamflow (SF) varies temporally throughout the year.

Fig. 15. The first graphic shows the temporal variation of spatially averaged recharge to groundwater for the entire watershed. The second figure is the spatial distribution of average annual recharge. We note that recharge is more often negative from July to Oct (with the exception of during and after storm events). This is the result of the significant negative potential created in unsaturated zone during the summer drought. On the other hand, localized high recharge rates (blue color, dark grey in black and white) are

observed where convergent topography focuses surface runoff and infiltration in high permeability or macroporous soils and bedrock. These are likely sites for wetland conditions.

Fig. 16. (a) Shows the percent of time each stream section is gaining (GS) during the period of simulation. Distribution of gaining and loosing sections of stream along with typical streamflow-aquifer dynamics for three cases viz. b) predominantly gaining, c) intermittently gaining and loosing and d) always loosing

Fig 17: Complexity of flow at stream junctions. Mouth of the tributaries that drain to a large and deep river are prone to be losing reaches, particularly in dry conditions because of large depression created by the main river. Similar behavior is observed at multiple locations (marked by bounded rectangles in top-left figure) across the watershed.

Fig 18: Nonlinear state effects on seasonal forcing. Two events of 10 day duration each, one from winter (Event 1) and the other from summer (Event 2), produce markedly different hydrographs as shown in (a) for Event 1 and (b) Event 2. (c-d) show that the total evapotranspiration loss during Event 2 is much larger than for 1. Thus the net available water for overland flow (e-f) and base flow (g-h) to the river is less for Event 2.

Fig. 19: Vertical cross-section of a subsurface control volume

Tables

Table 1. Definition of coupling function and the lateral and vertical fluxes across the faces of a control volume. i and j are indices of neighboring control volumes and $\| \ \|$ denotes conditional terms which exist only for the grids that are neighbor of a river element. Explanation of symbols is in Appendix I.

Table 2. Effective macroporous-soil infiltration rate modeled as a dual matrix-macropore system for different water application rate conditions. $\vec{G}_{0mat}$ and $\vec{G}_{0mac}$ are matrix and macropore infiltration rates. Explanation of symbols is in Appendix I

Table 3: A-priori distributed data requirements for a PIHM model simulation and the sources from which distributed parameters were derived.

Table 1. Definition of coupling function and the lateral and vertical fluxes across the faces of a control volume. i and j are indices of neighboring control volumes and $\| \ \|$ denotes conditional terms which exist only for the grids that are neighbor of a river element. Explanation of symbols is in Appendix I.

Prismatic Element					
Control Volume	$\overline{\psi}$ (State)	$\vec{G}$ (Vertical Flux)	$\vec{F}$ (Horizont-al Flux)	$\overline{S}_{\psi}$ (Source/ Sink)	$f[]$ (Coupling Flux Function)
Interception	ψ_0	$\vec{G}_3 - \vec{G}_4 - \vec{G}_5$	--	--	$\vec{G}_5 \equiv \mathrm{f}[\psi_0]$
Snow	ψ_1	$\vec{G}_3 - \vec{G}_6$	--	--	$\vec{G}_6 \equiv \mathrm{f}[\psi_1]$
Surface Flow	ψ_2	$\vec{G}_3 - \vec{G}_0 - \vec{G}_7 + \vec{G}_5 + \vec{G}_6$	$\vec{F}_0 + \left\|\vec{F}_1\right\|$	--	$\vec{F}_0 \equiv \mathrm{f}[\psi_{2i}, \psi_{2j}], \vec{G}_0 \equiv \mathrm{f}[\psi_2, \psi_3]$ $\vec{G}_5 \equiv \mathrm{f}[\psi_0], \vec{G}_6 \equiv \mathrm{f}[\psi_1], \left\|\vec{F}_1\right\| \equiv \mathrm{f}[\psi_5, \psi_2]$
Unsaturated Zone	ψ_3	$\vec{G}_0 - \vec{G}_1 - \vec{G}_8 - \vec{G}_9$	--	--	$\vec{G}_0 \equiv \mathrm{f}[\psi_2, \psi_3], \vec{G}_1 \equiv \mathrm{f}[\psi_3, \psi_4]$ $\vec{G}_8 \equiv \mathrm{f}[\psi_3], \vec{G}_9 \equiv \mathrm{f}[\psi_3, \psi_0]$
Saturated Zone	ψ_4	$\vec{G}_1$	$\vec{F}_2 + \left\|\vec{F}_3\right\| + \left\|\vec{F}_4\right\|$	$-S_1$	$\vec{G}_1 \equiv \mathrm{f}[\psi_3, \psi_4], \vec{F}_2 \equiv \mathrm{f}[\psi_{4i}, \psi_{4j}]$ $\left\|\vec{F}_3\right\| \equiv \mathrm{f}[\psi_5, \psi_4], \left\|\vec{F}_4\right\| \equiv \mathrm{f}[\psi_6, \psi_4)]$
Linear Element					
Channel zone	ψ_5	$\vec{G}_3 - \vec{G}_2 - \vec{G}_7$	$\left\|\vec{F}_3\right\| + \vec{F}_5 + \left\|\vec{F}_1\right\|$	--	$\vec{G}_2 \equiv \mathrm{f}[\psi_5, \psi_6], \vec{F}_5 \equiv \mathrm{f}[\psi_{5i}, \psi_{5j}]$ $\vec{F}_1 \equiv \mathrm{f}[\psi_5, \psi_2], \left\|\vec{F}_3\right\| \equiv \mathrm{f}[\psi_5, \psi_4]$
Sub-Channel Zone	ψ_6	$\vec{G}_2$	$\left\|\vec{F}_4\right\|$	--	$\left\|\vec{F}_4\right\| \equiv \mathrm{f}[\psi_6, \psi_4], \vec{G}_2 \equiv \mathrm{f}[\psi_5, \psi_6]$

Table 2. Effective macroporous-soil infiltration rate modeled as a dual matrix-macropore system for different water application rate conditions. $\vec{G}_{0\,mat}$ and $\vec{G}_{0\,mac}$ are matrix and macropore infiltration rates. Explanation of symbols is in Appendix I

Condition	$\vec{G}_{0\,mat}$	$\vec{G}_{0\,mac}$
$\psi_3 = z - z_b - \psi_4$	$K_{matV}[S=1](1-\beta)grad\,\psi$	$K_{macV}[S=1]\beta gr$
$\vec{G}_0 < K_{matV}[S]$	$\vec{G}_0$	---
$\vec{G}_0 > K_{matV}[S]$ and $\vec{G}_0 < K_{\max}$	$K_{matV}[S](1-\beta)grad\,\psi$	$K_{macV}[S]\beta grad\,\psi$
$\vec{G}_0 > K_{matV}[S]$ and $I > K_{\max}$	$K_{matV}[S](1-\beta)grad\,\psi$	$K_{macV}[S=1]\beta gr$

Table 3: A-priori distributed data requirements for a PIHM model simulation and the sources from which distributed parameters were derived.

Feature/ Time Series	Property	Source
Soil	Porosity; Sand, Silt, Clay Fractions; Bulk Density	CONUS, SSURGO and STATSGO http://www.soilinfo.psu.edu/index.cgi?soil_data&conus http://datagateway.nrcs.usda.gov/NextPage.asp http://www.ncgc.nrcs.usda.gov/products/datasets/statsgo/
Geology	Bed Rock Depth; Horizontal and Vertical Hydraulic Conductivity	http://www.dcnr.state.pa.us/topogeo/, http://www.lias.psu.edu/emsl/guides/X.html
Land Cover	LAI	http://glcf.umiacs.umd.edu/data/landcover/data.shtml, http://ldas.gsfc.nasa.gov/LDAS8th/MAPPED.VEG/LDASmapveg.shtml;
	Manning's Roughness	Hernandez et. al., 2000
River	Topology: From Node – To Node, Neighboring Elements;	Derived using PIHMgis (Bhatt et. al., 2008)
	Manning's Roughness;	Dingman (2002)
	Coefficient of Discharge	ModHms Manual (Panday and Huyakorn, 2004)
	Shape and Dimensions;	Derived from regression using depth, width and discharge data from http://nwis.waterdata.usgs.gov/usa/nwis/measurements
Forcing	Precipitation, Temperature	Gauge data obtained from MARFC. 6 hourly precipitation point data is spatially gridded such that it conforms to the monthly precipitation distribution map obtained from parameter-elevation regressions on independent slopes model (PRISM) (Daly et. al., 1994, 1997)
DEM		http://seamless.usgs.gov/
Streamflow		http://nwis.waterdata.usgs.gov/nwis/sw
Groundwater		http://nwis.waterdata.usgs.gov/nwis/gw

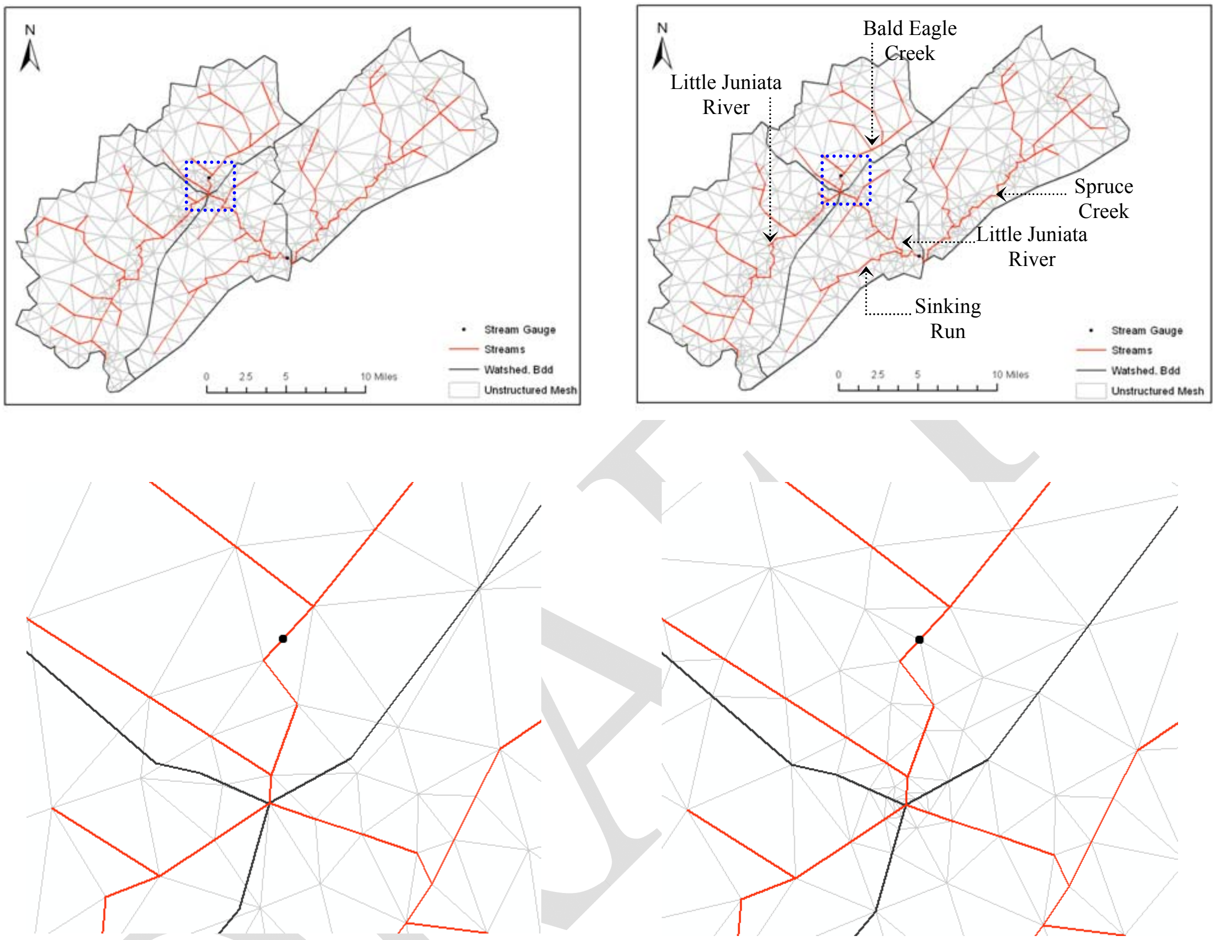

Fig. 1. Unstructured domain decomposition of Little Juniata Watershed generated with (right) and without (left) the use of subwatershed boundaries and streamflow observation station as constraints. Note that in decomposition with the constraints, the observation station acts as a node of the river discretization element (right). The modeled flux location will be exactly at the gauge location thus appropriately accounting for the exact contributing area. Also the mesh boundary coincides with subwatershed boundaries (right) thus preserving necessary surface water flow directions.

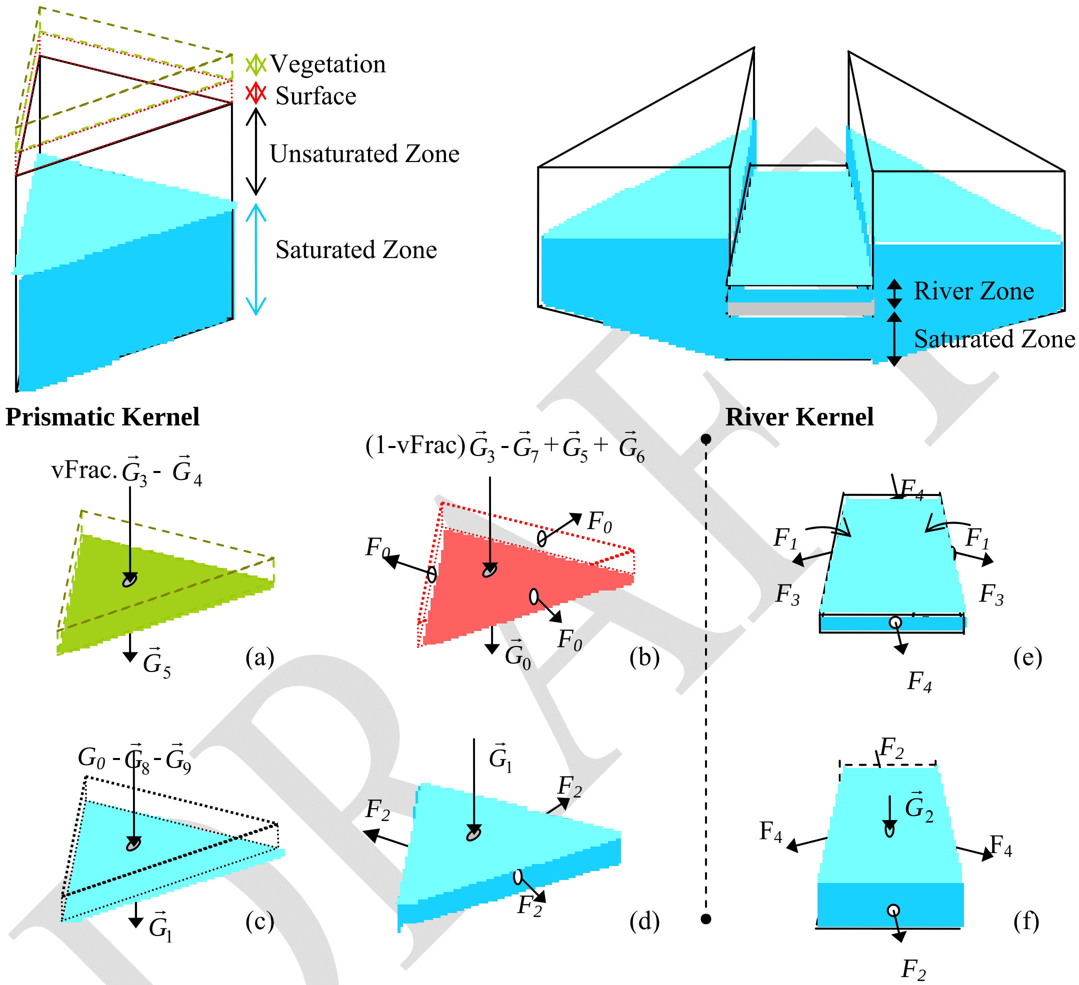

Fig. 2. Prismatic (top left) and linear River (top right) kernels constitute a model domain. We note that each linear river kernel is sandwiched between neighboring watershed prismatic kernel elements. A kernel is a stack of control volumes corresponding to different states. Process interactions across the control volumes faces (listed in Table 1) are also shown. Sub-paneled graphics correspond to control volumes for a) Vegetation b) Overland Flow c) Unsaturated Zone d) Saturated Zone e) River flow and f) Groundwater flow below river bed.

.

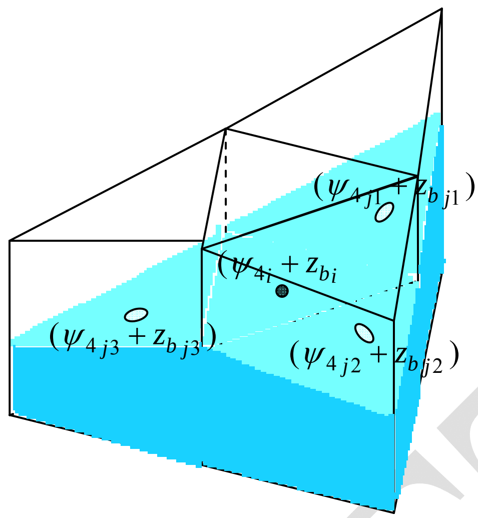

Fig. 3: Groundwater flux across all the three prismatic kernel edges depends on the head gradient across it

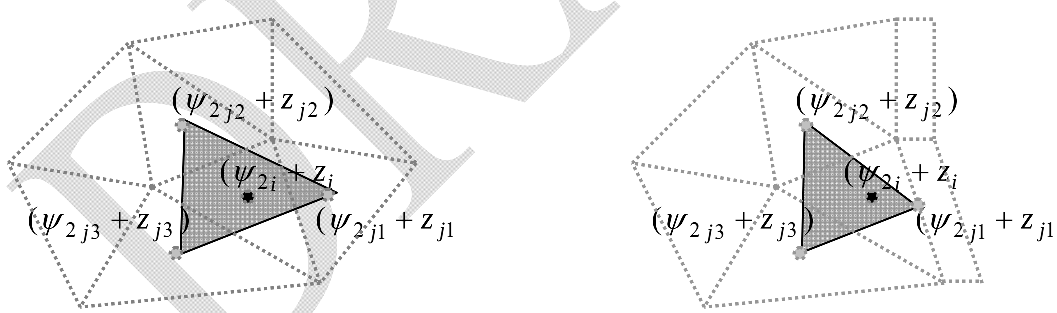

Fig. 4. $\nabla_s \psi$ for the unit element i in Eq. (13) is calculated by approximating a triangular stencil over neighboring elements. The graphic on the right addresses the case when a prismatic element neighbors a river. The expression for the gradient is in Appendix II.

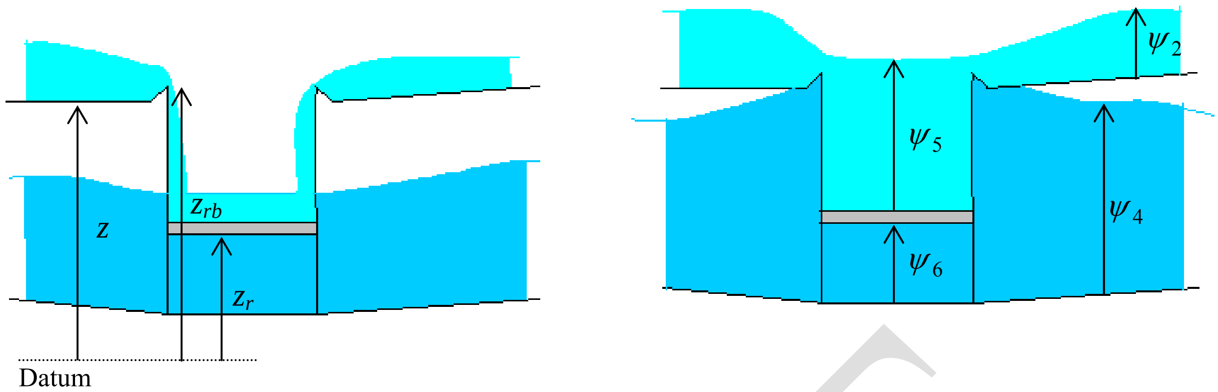

Fig. 5. Two cases of surface flow across the "weir/dam" type channel bank. Case on the left pertains to when river stage is lower than the river bank height while case on the right has river stage larger than the bank height. We note that for the both cases shown above, $(\psi + z)_u$ in Eq. (15) will be (z+ψ_2)

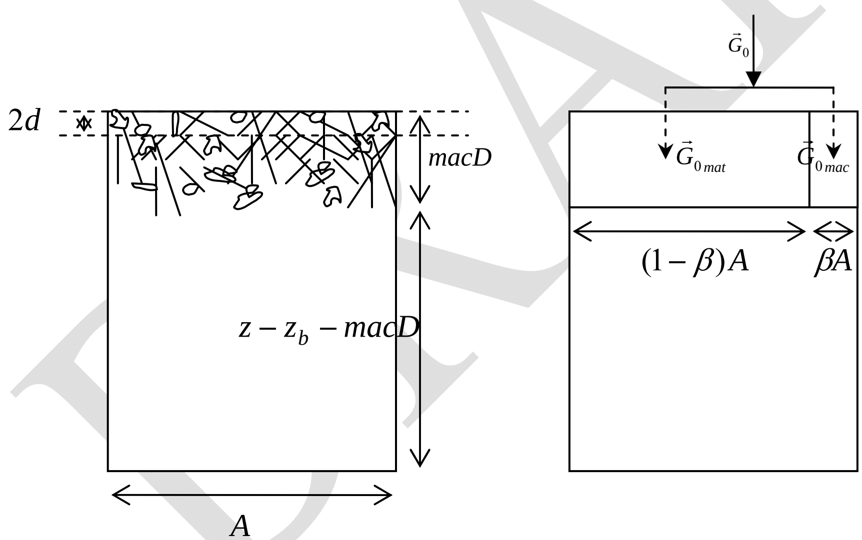

Fig. 6. Graphic on the left shows how PIHM defines the depth of macropores (*macD*). The surface "skin-depth" *2d* is defined as the depth over which the infiltration is calculated. The conceptual model of infiltration/exfiltration based flow is shown in the right graphic where the system is divided into a dual matrix with micropore and macropore media

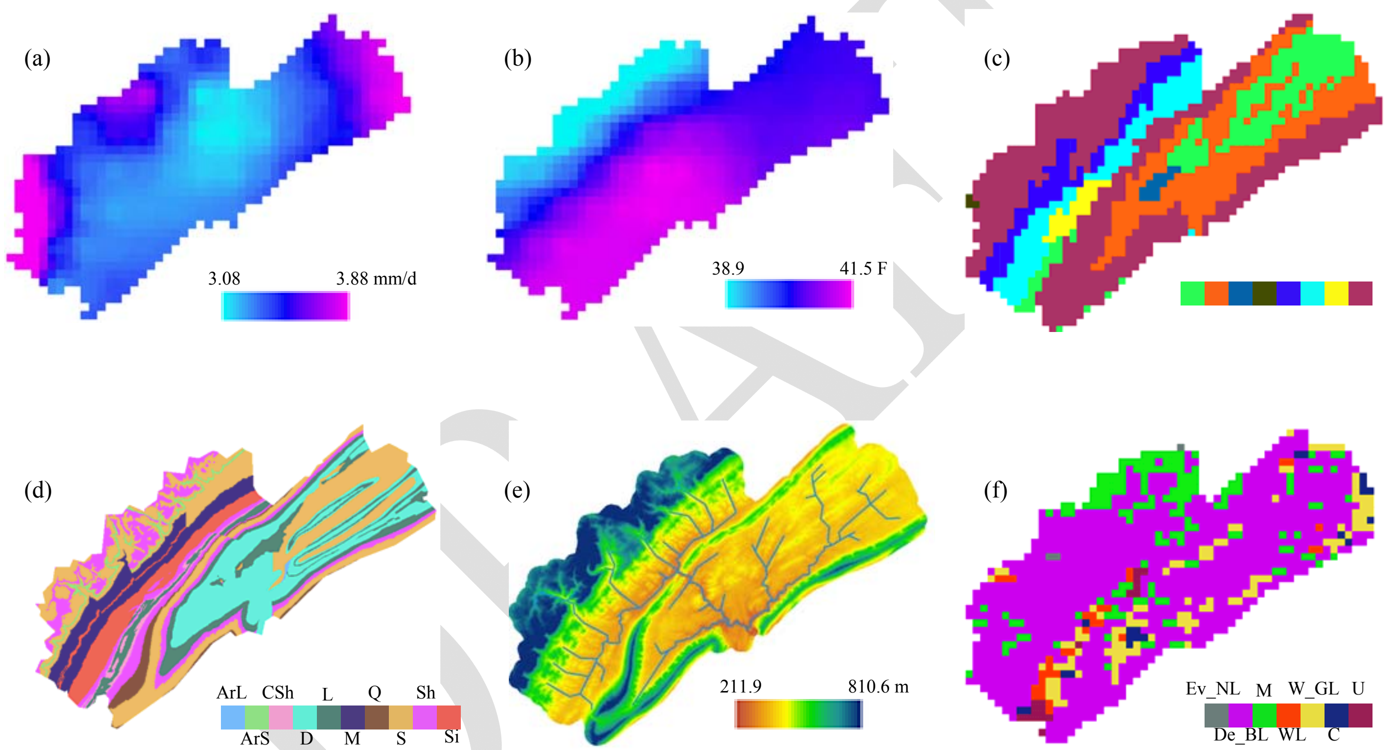

Fig. 7. Distributed data map of a) Precipitation (Nov, 1983) b) Temperature (Nov, 1983) c) Soils d) Geology e) Elevation and f) Land Cover for Little Juniata Watershed. Data sources are listed in Table 3

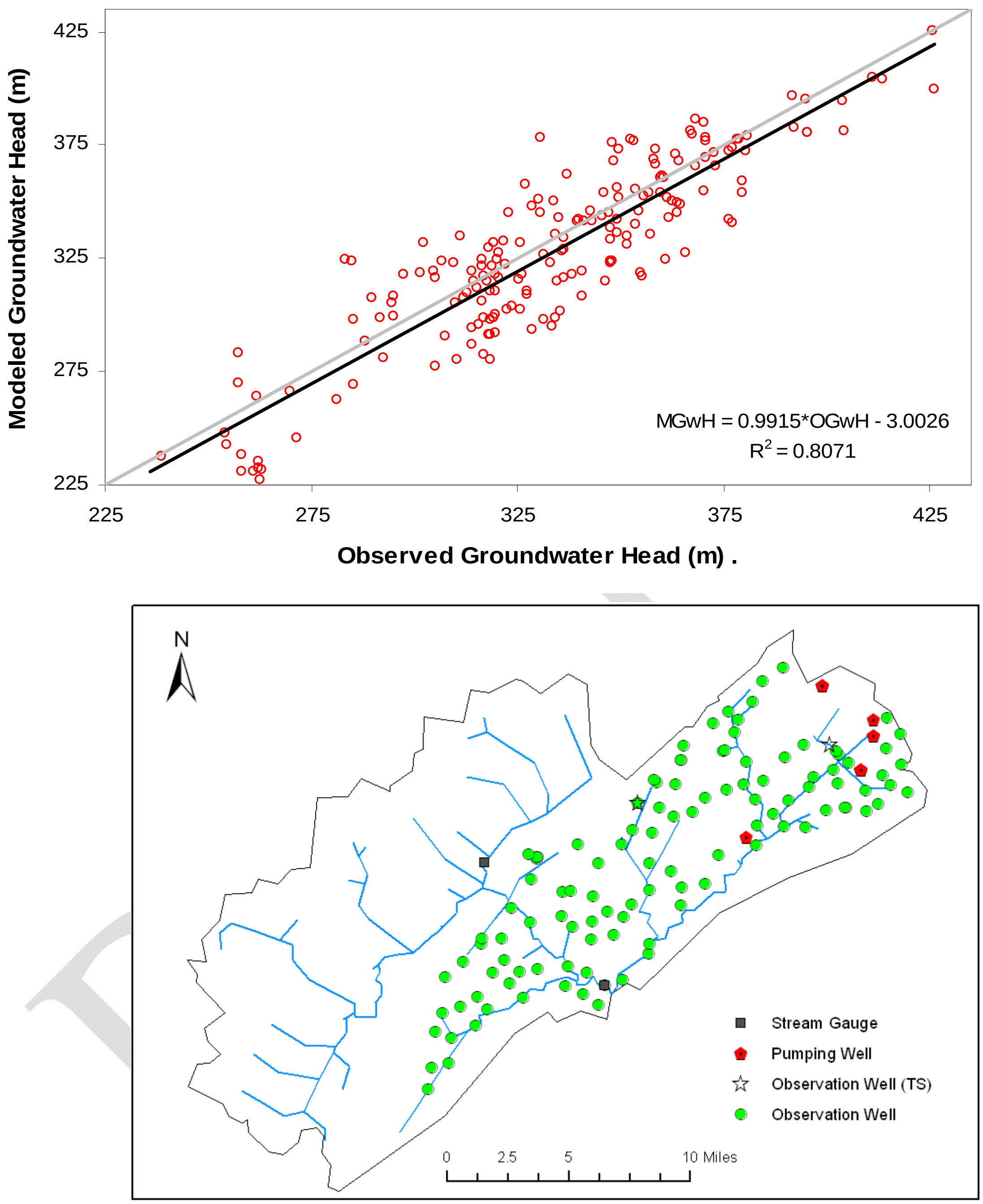

Fig. 8. Modeled groundwater head (MGwH) vs. Observed groundwater head (OGwH) for the observation wells (shown in the lower graphic) for the 1983 -84 period of the model run. Data source for observed head: http://nwis.waterdata.usgs.gov/nwis/gw

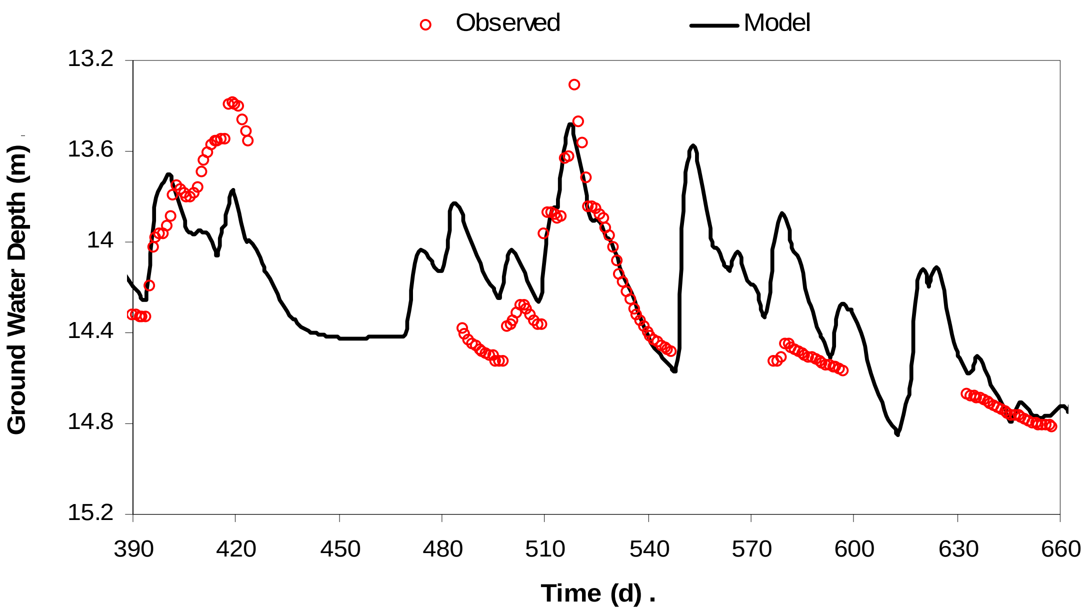

Fig. 9. Modeled and Observed ground water depth time series. Data source for observed head: http://nwis.waterdata.usgs.gov/nwis/gw

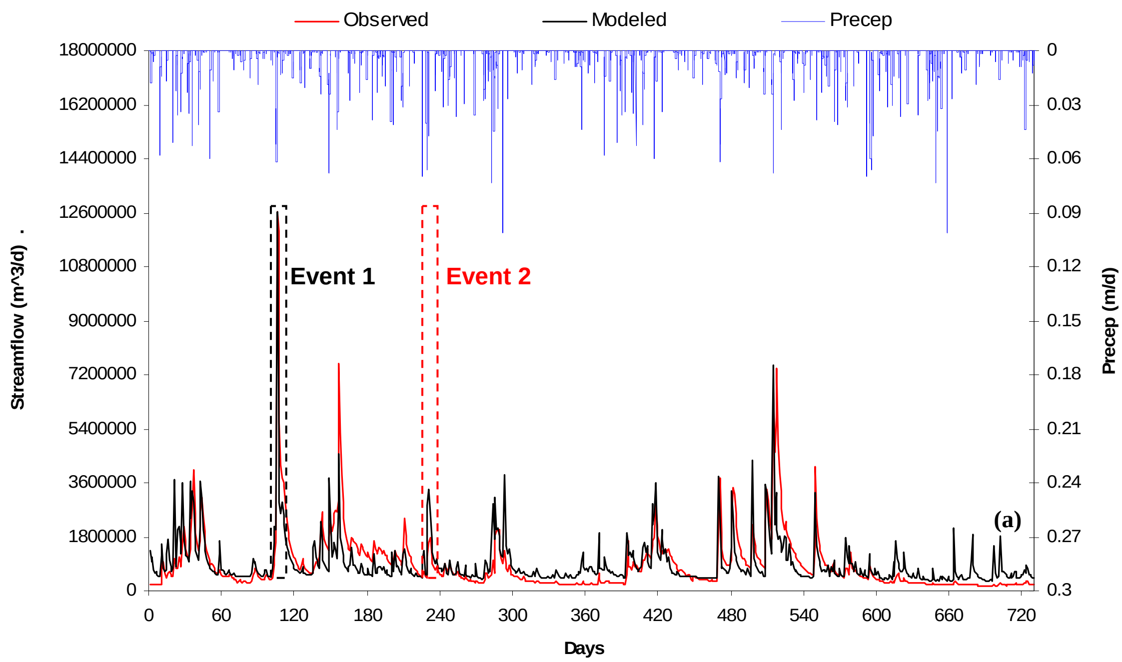

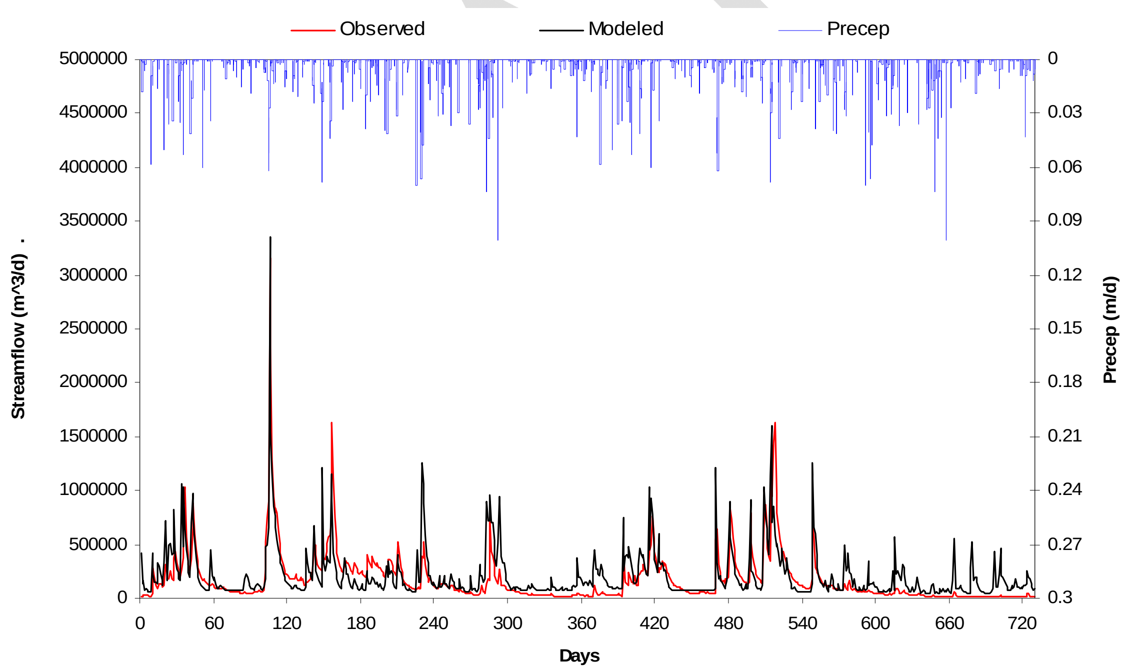

Fig. 10. Observed and Modeled Streamflow at a) Little Juniata River Observation Station b) Bald Eagle Creek Observation station. Data source for observed head: http://nwis.waterdata.usgs.gov/nwis/sw

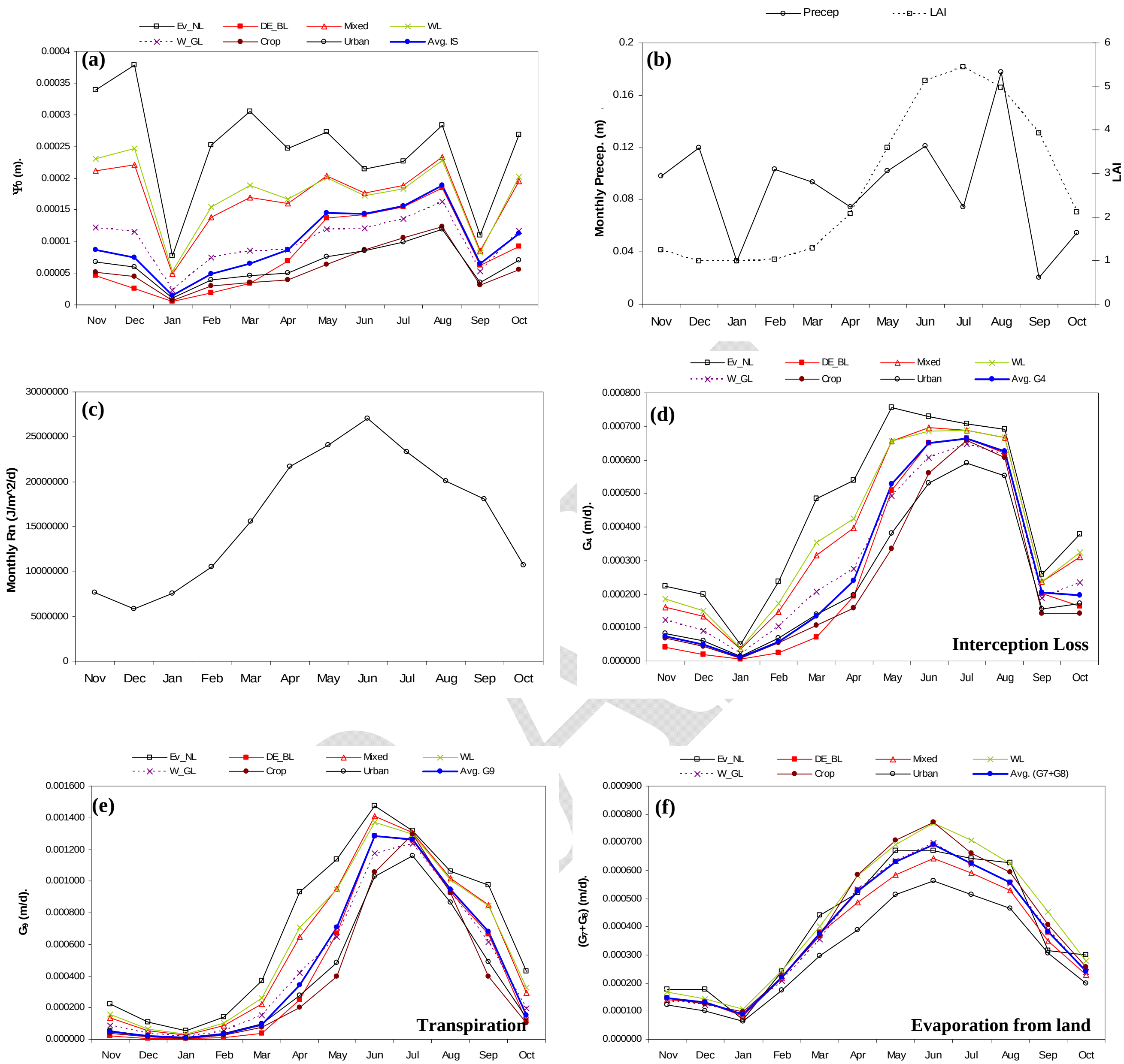

Fig. 11. a) Average monthly interception storage for different land cover types. Expectedly, variation in interception storage is correlated with precipitation. b) Variation of monthly precipitation and LAI. c) Monthly average of incoming solar radiation d) Monthly aveage of evaporation from interception storage ($\vec{G}_4$) shows signatures of its dependence on interception storage (maximum in August) and Incoming solar radiation (maximum in June e) Temporal variation in monthly transpiration ($\vec{G}_9$) has a strong dependence on LAI and radiation. f) Monthly evaporation from overland flow and the upper soil layer ($\vec{G}_7 + \vec{G}_8$) is found to follow annual cycle of temperature and radiation

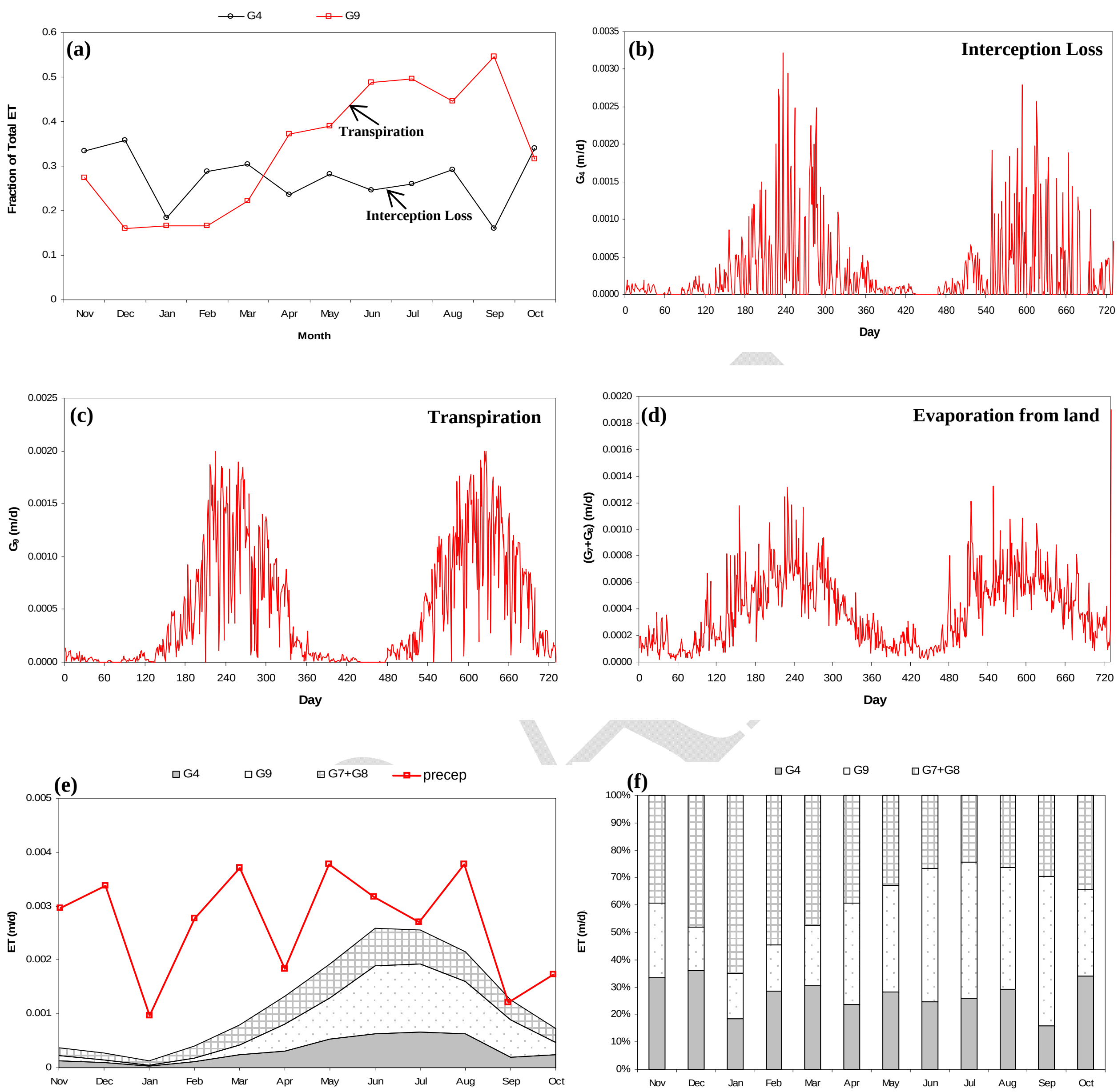

Fig 12: a) Variation of fractional loss components (transpiration and interception loss) with respect to total evapotranspiration. We note that when fraction of transpiration to total evapo-transpiration increases, the corresponding fraction of interception loss decreases and vice-versa. b) Annual variation of daily interception loss rate, $\vec{G}_4$ (Annual average $\vec{G}_4$ = 0.000288 m/d) c) Annual variation of daily transpiration loss rate, $\vec{G}_9$ (Annual average $\vec{G}_9$ = 0.000466 m/d) d) Annual variation of daily evaporation rate from ground, $\vec{G}_7 + \vec{G}_8$ (Annual average $\vec{G}_7 + \vec{G}_8$ = 0.000387 m/d). e) Average monthly precipitation and evapotranspirative loss f) Relative percentage contribution of each evapo-transpirative flux component

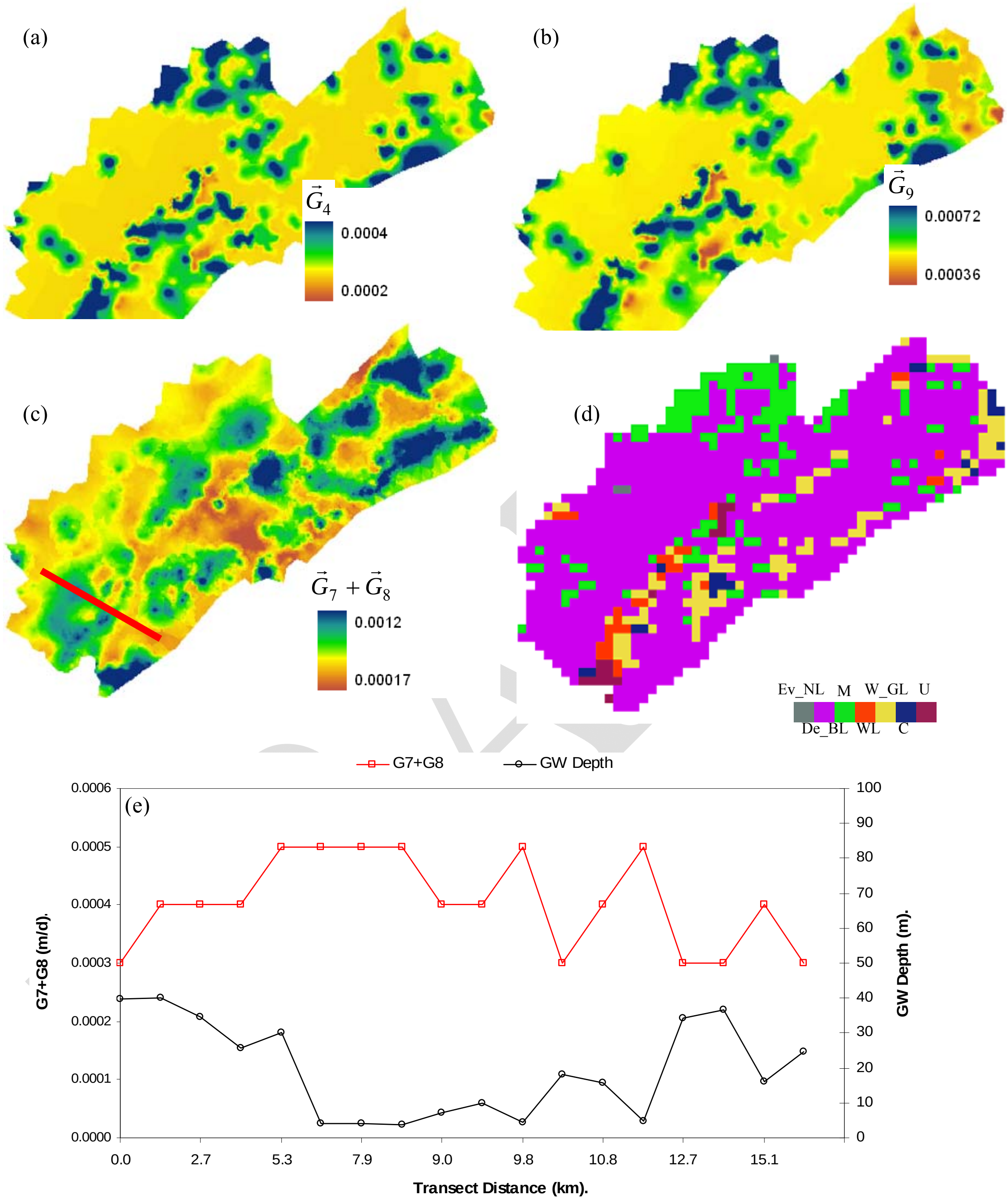

Fig. 13. Spatial pattern of annual average evaporation from a) canopy and b) transpiration closely reflect the vegetation pattern. (shown in (d)). Spatial pattern of ground evaporation (shown in (c)) strongly depends on the depth of ground water and recharge pattern. Figure (e) shows that the variation of evaporation from ground ($\vec{G}_7 + \vec{G}_8$) along a transect across the valley (shown as a rectangular strip in (c)) follows an inverse relationship to ground water depth (and elevation).

$\vec{G}_7 + \vec{G}_8$ are larger where there are shallow groundwater conditions (at lower elevations) and vice-versa

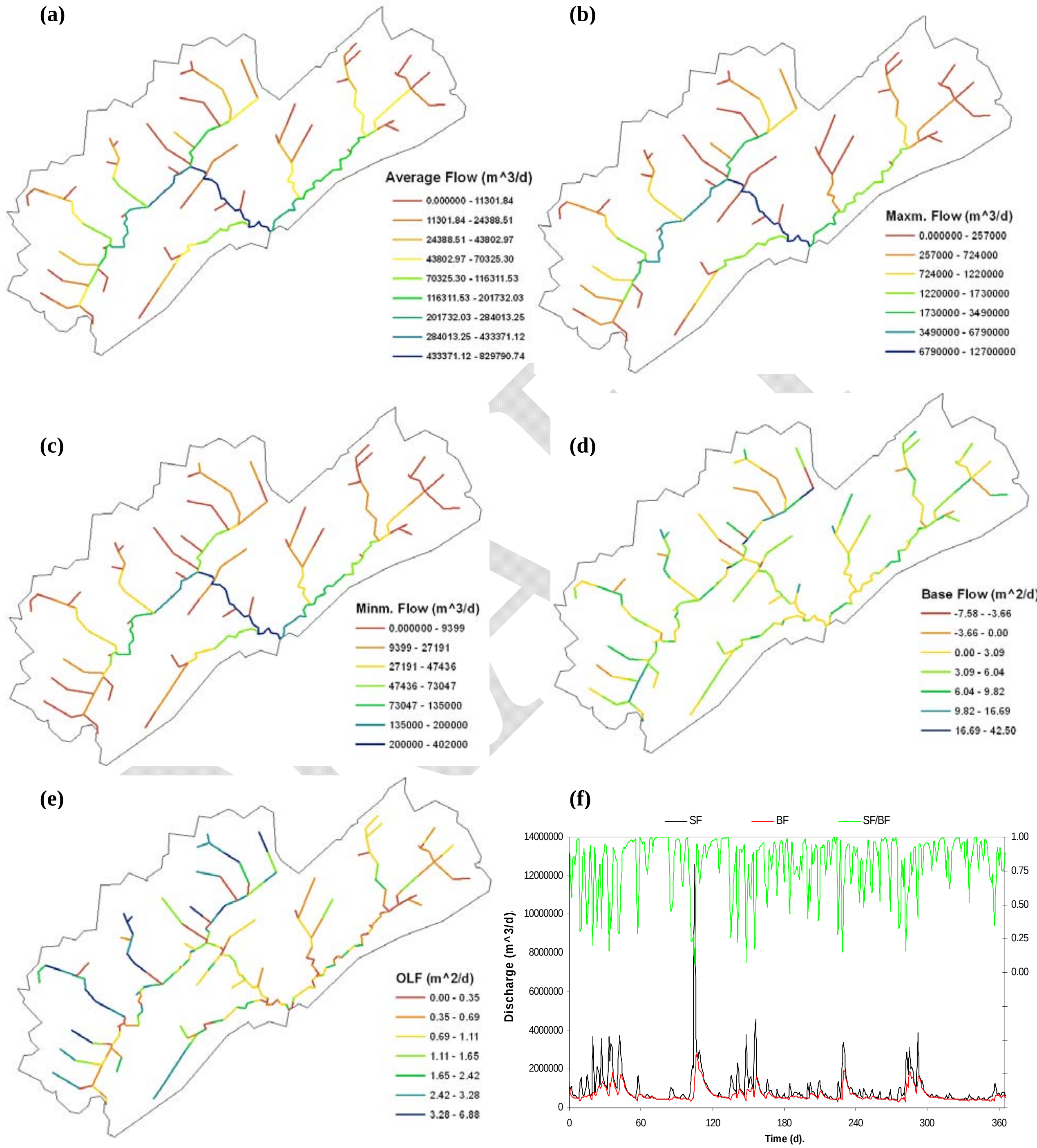

Fig. 14. (a) Spatial distribution of annual average flow in the stream network of Little Juniata Watershed. b) Maximum and c) minimum flow in each section of river. d) Baseflow (BF) and e) overland flow (OLF) contribution to river per unit length of stream varies heterogeneously

depending on local topography and hydrogeologic properties. f) Base flow contribution (BF) to total streamflow (SF) varies temporally throughout the year

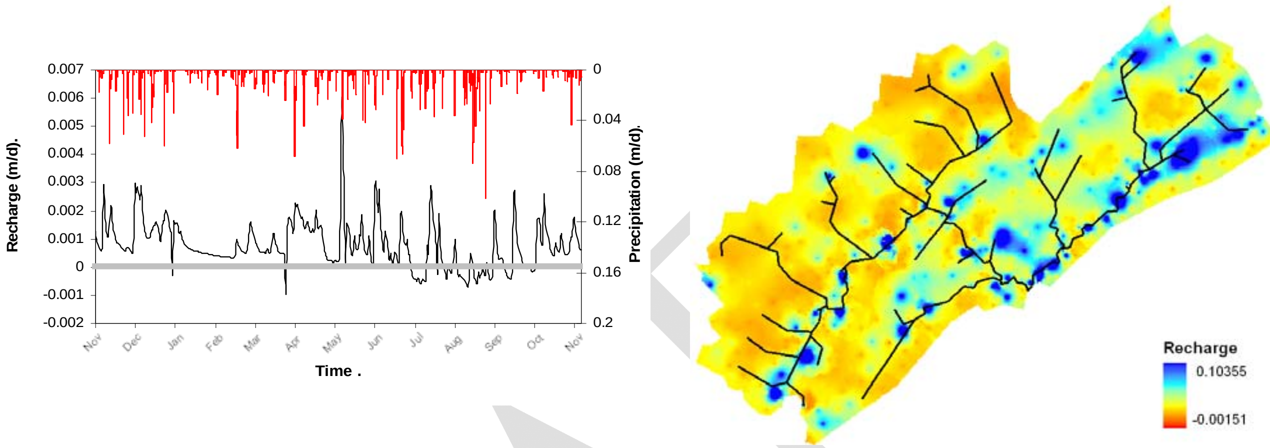

Fig. 15. The first graphic shows the temporal variation of spatially averaged recharge to groundwater for the entire watershed. The second figure is the spatial distribution of average annual recharge. We note that recharge is more often negative from July to Oct (with the exception of during and after storm events). This is the result of the significant negative potential created in unsaturated zone during the summer drought. On the other hand, localized high recharge rates (blue color, dark grey in black and white) are observed where convergent topography focuses surface runoff and infiltration in high permeability or macroporous soils and bedrock. These are likely sites for wetland conditions.

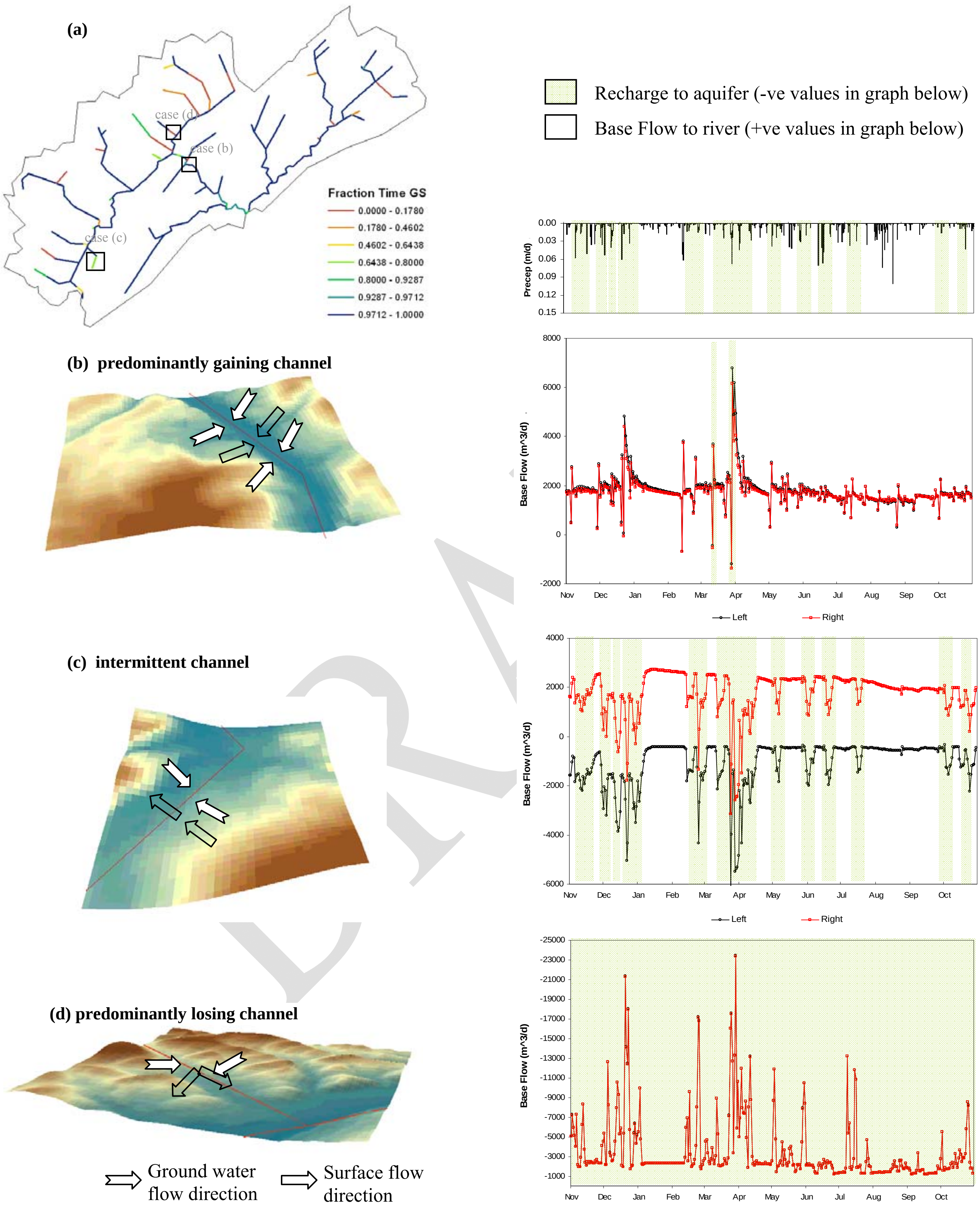

Fig. 16. (a) Shows the percent of time each stream section is gaining (GS) during the period of simulation. Distribution of gaining and loosing sections of stream along with typical streamflow-aquifer dynamics for three cases viz. b) predominantly gaining, c) intermittently gaining and loosing and d) always loosing

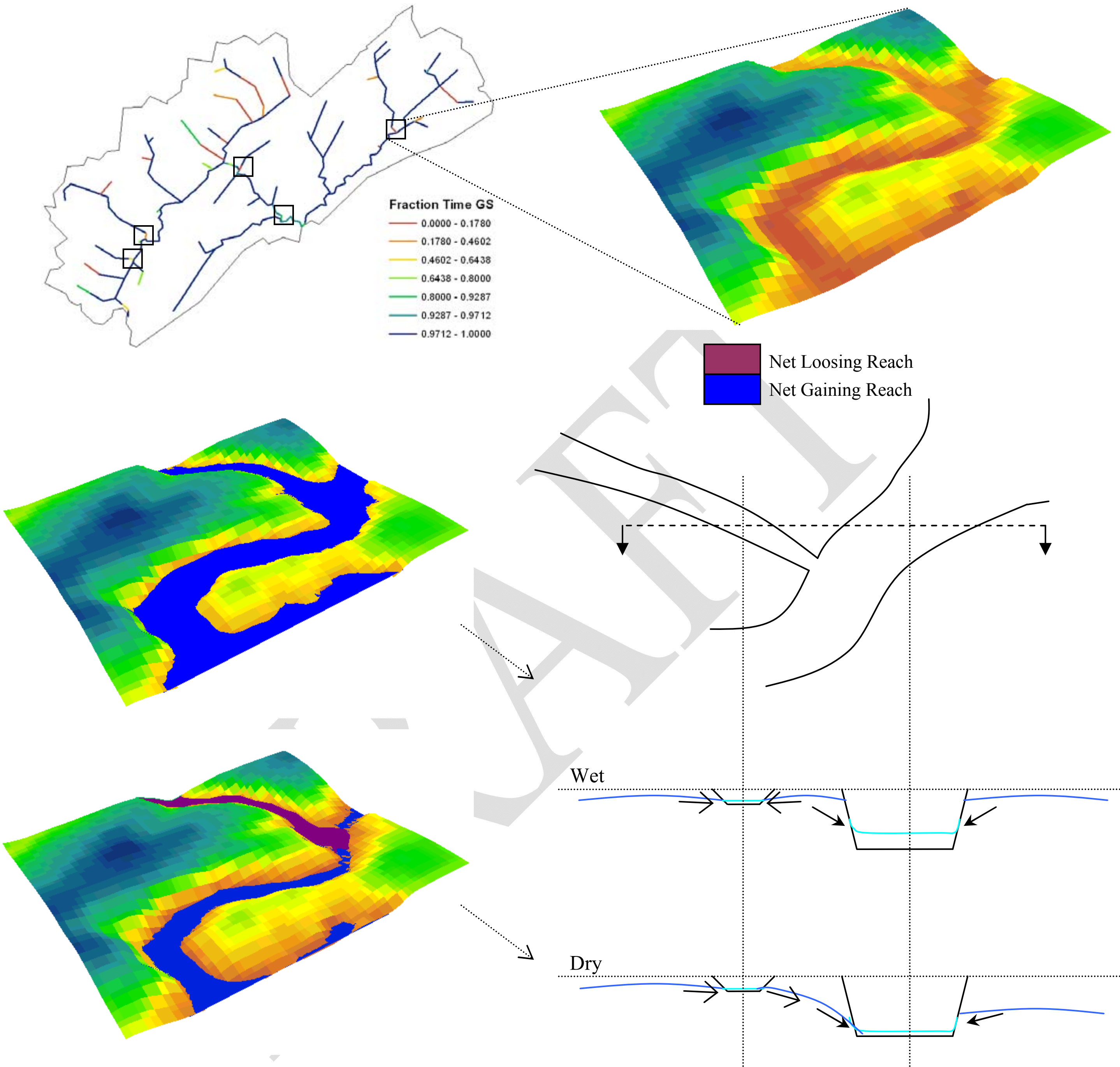

Fig 17: Complexity of flow at stream junctions. Mouth of the tributaries that drain to a large and deep river are prone to be losing reaches, particularly in dry conditions because of large depression created by the main river. Similar behavior is observed at multiple locations (marked by bounded rectangles in top-left figure) across the watershed.

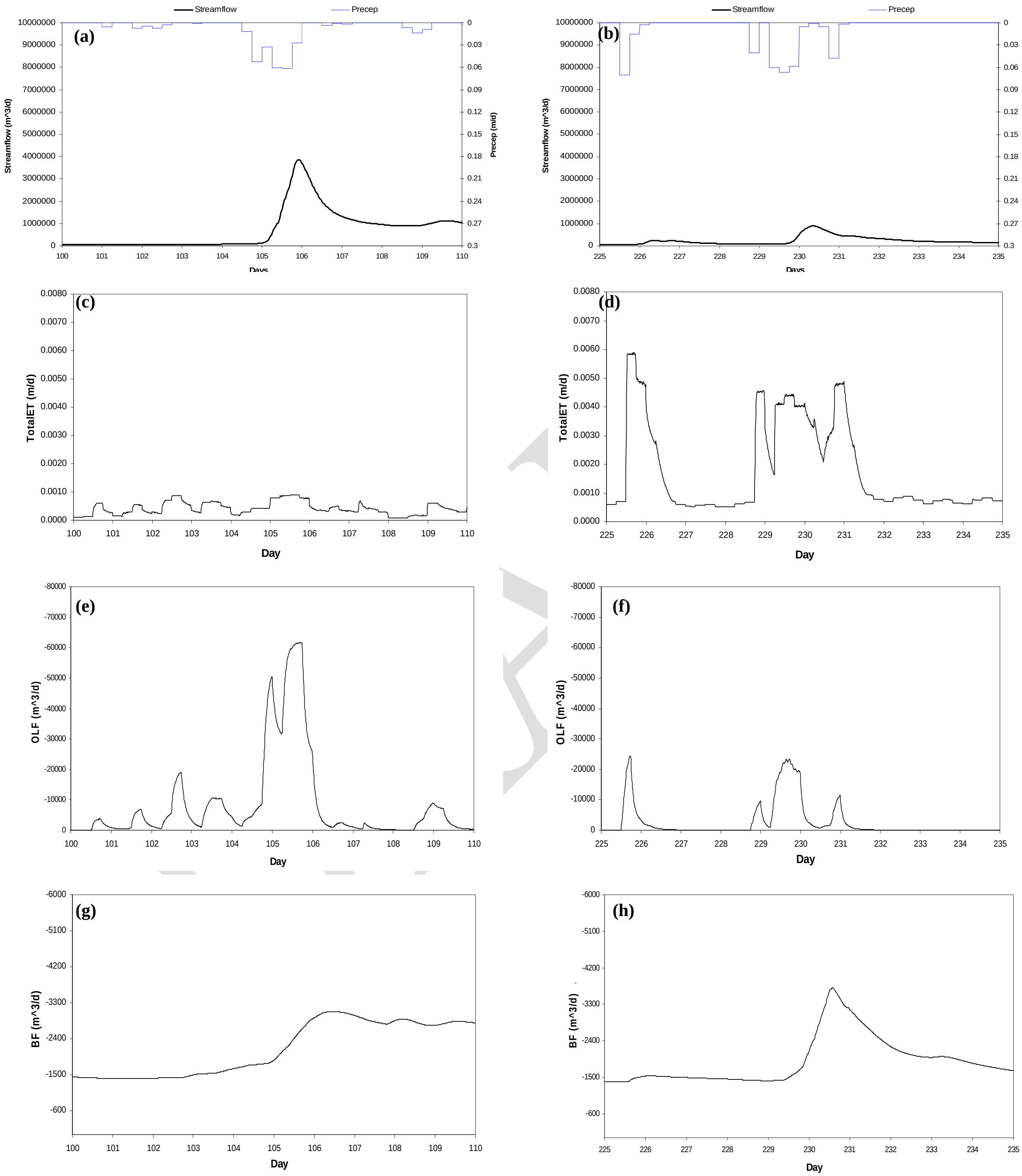

Fig 18: Nonlinear state effects on seasonal forcing. Two events of 10 day duration each, one from winter (Event 1) and the other from summer (Event 2), produce markedly different hydrographs as shown in (a) for Event 1 and (b) Event 2. (c-d) show that the

total evapotranspiration loss during Event 2 is much larger than for 1. Thus the net available water for overland flow (e-f) and base flow (g-h) to the river is less for Event 2.

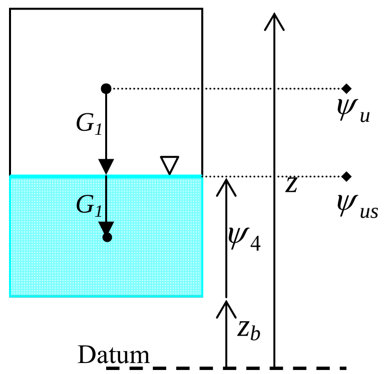

Fig. 19: Vertical cross-section of a subsurface control volume